Commun. Comput. Phys.
doi: 10.4208/cicp.OA-2024-0087

Vol. **37**, No. 1, pp. 61-103
January 2025

Lattice Boltzmann Modeling of Non-Newtonian Fluid Flows Under Non-Linear Slip Velocity Boundary Conditions in Microchannels

Francisco Reis[1], Goncalo Silva[2,*] and Viriato Semiao[1]

[1] *IDMEC, Departamento de Engenharia Mecânica, Instituto Superior Tecnico, Universidade de Lisboa, Av. Rovisco Pais 1, 1049-001, Lisboa, Portugal.*
[2] *IDMEC, Departamento de Engenharia Mecatrónica, Escola de Ciências e Tecnologia, Universidade de Évora, R. Romão Ramalho 59, 7000-671 Évora, Portugal.*

Received 13 April 2024; Accepted (in revised version) 6 October 2024

Abstract. Fluid flows in microfluidic devices are often characterized by non-Newtonian rheology with non-linear wall slip behavior also observed. This work solves this problem class with the lattice Boltzmann method (LBM), proposing new advanced boundary scheme formulations to model the joint contribution of non-linear rheology and non-linear wall slip laws in application to microchannels of planar and circular cross-section. The non-linear stress-strain-rate relationship of the microflow is described by a generalized Newtonian model where the viscosity function follows the Sisko model. To guarantee that LBM steady-state solutions are not contaminated by numerical errors that depend on the viscosity local value, the two-relaxation-time (TRT) collision is adopted. The fluid-wall accommodation model considers different slip laws, such as the Navier linear, Navier non-linear, empirical asymptotic and Hatzikiriakos slip laws. They are transcribed into the LBM framework by adapting the local second-order boundary (LSOB) scheme strategy to this problem class. Theoretical and numerical analyses developed for a steady and slow viscous fluid within 2D slit and 3D circular pipe channels demonstrate the parabolic level of accuracy of the developed LSOB scheme throughout the considered non-linear slip and non-Newtonian models.

AMS subject classifications: 76-04, 76P05, 65Z05
Key words: Lattice Boltzmann method, two-relaxation-time scheme, slip velocity boundary conditions, non-Newtonian fluids.

1 Introduction

Boundary slip phenomenon has received growing attention in both gas [1–3, 7] and liquid [4–7] flows in most part motivated by the development of micro- and nano-scale

*Corresponding author. *Email addresses:* gnsilva@uevora.pt (G. Silva), franciscoda@tecnico.ulisboa.pt (F. Reis), viriatosemiao@tecnico.ulisboa.pt (V. Semiao)

technologies [8]. With the scale reduction, the interaction between the fluid and the solid wall starts to exhibit physical mechanisms that deviate from the well-established no-slip velocity boundary condition [9] and that affects both gas and liquid flows.

Gas slip is typically promoted by fluid rarefaction. This property is quantified by the flow Knudsen number $\mathrm{Kn}=\lambda/L$, where λ is the gas mean-free-path (a microscopic length scale) and L is a characteristic dimension of the flow domain (a macroscopic length scale). Commonly, the slip flow regime is defined at $0.001 \leq \mathrm{Kn} \leq 0.1$, where the application of conventional hydrodynamics equations remains valid, but the no-slip velocity condition needs to be replaced by one that accounts for slip effects [10], e.g., as given by the wall slip model proposed by Maxwell [11]. When gas rarefaction is increased over $\mathrm{Kn} > 0.1$, besides the wall slip effect, new flow features need to be considered, most notably the Knudsen layers, which further modify the gas flow topology [10]. The macroscopic description of such Knudsen layers is often performed through a non-linear stress-strain-rate relationship, whose mathematical formulation is similar to that of a non-Newtonian fluid [2, 3, 12]. Moreover, in the presence of high shear rates, the fluid-solid interaction model of the rarefied gas also needs to take into account the non-linear nature of the underlying physics. This process is best described by non-linear slip velocity boundary conditions [7]. The inclusion of the combined effects between non-Newtonian rheology and non-linear slip laws is therefore crucial for the accurate macroscopic modelling of gaseous flows at moderate Kn regimes. These phenomena are frequently encountered in microfluidic gas flow applications, such as microfluidic gas sensors or actuators and micro-propulsion devices [13].

Liquid slip can be found in a wide variety of physical instances. Applications range from the transport of water in tight sandstones and of oil in shale matrices [14] to low drag hydrophobic surfaces [15], or industrial appliances related to polymer processes [16]. For these latter, the interplay between fluid rheology and boundary accommodation is even richer as it gives rise to different types and mechanisms of wall slip phenomena [4, 16]. This work intends to advance the numerical modeling of such physical phenomena, which in the case of liquids are characterized by the dimensionless slip length $\zeta = b/L$ that quantifies the ratio between the slip length b and the flow characteristic dimension L [7]. In fact, there is large experimental evidence suggesting that in the aforementioned application fields the liquid substances flowing inside narrow pores or in tiny capillaries are more accurately treated as "dense molecular fluids" [6]. At macroscopic level, these are best described by continuum flow models that simultaneously consider non-Newtonian rheological laws with non-linear slip boundary conditions [7, 16].

Unfortunately, analytical solutions to this slip flow problem class are scarce, even at the simplest flow settings [16, 17]. As a result, studies in this field tend to become only accessible through numerical simulations. For this purpose, most computational efforts have been devoted to the finite element method (FEM) [18, 19] or the finite volume method (FVM) [20, 21] as numerical techniques. However, considering the appealing numerical characteristics of the lattice Boltzmann method (LBM) as alternative computational fluid dynamics (CFD) technique, particularly in the modeling of complex fluid

flow phenomena [22–24], this work proposes exploring the application of the LBM for the numerical modeling of Newtonian and non-Newtonian fluids subject to linear and non-linear wall slip conditions in microchannel flow problems.

Historically, the development of LBM boundary schemes to implement the slip velocity condition at walls has been the subject of extensive literature studies, e.g. [25–37], which cover a broad range of physical settings, from gas [25, 27, 33, 34] to liquid [41, 42] flows, also including multi-phase/multi-component systems [38–40], applying along both straight [25–29, 33] and curved [31, 34, 35, 37] surfaces. However, to the best of the authors knowledge, all these studies share the common limitation that they only consider linear slip models, either in the form of Maxwell [11] or Navier [43] slip laws. So far, the formulation of LBM boundary schemes that account for non-linear slip laws has been overlooked, although the non-linear slip boundary condition is oftentimes fundamental in the correct modeling of flows under micro- or nano-scale confinement [6], even under low to moderate shear conditions, as previously mentioned. To fill this gap, the first purpose of this work is to develop LBM boundary schemes that model linear and non-linear slip laws.

At the same time, it is also well-recognized that the behavior of fluid flows under micro- or nano-scale confinement commonly deviates from that of a Newtonian fluid [45]. Rather, it is often necessary to include a non-linear stress-strain-rate relationship in the fluid rheological model. This work will consider this relationship in the form of the generalized Newtonian model with the viscosity function given by Sisko [46] model, which is a generalization of the power law viscosity model [47]. Although these and other relatable rheological models have been implemented and studied over a variety of LBM collision models, such as single-relaxation-time [48–51], regularized-based [52], two-relaxation-time [53], multiple-relaxation-time [54–57], central-moment-based [58, 59], and lattice kinetic schemes [60], to the best of our knowledge, a dedicated analysis on how the LBM scheme accommodates the non-Newtonian fluid onto a solid boundary is still currently missing from literature. This issue is not of small importance as it is well-known that some LBM models are prone to viscosity-dependent numerical errors, which inevitably propagate towards boundary sites leading to an unphysical viscosity-dependent numerical slip on the wall boundary condition [61, 62]. In bulk, it has been proven [63] that the use of the two-relaxation-time (TRT) [64, 65] or the multiple-relaxation-time (MRT) [66] collision models permits fixing the LBM numerical errors independent from the assigned viscosity magnitude. While the satisfaction of this property is obviously important for general fluid flows, it is even more pressing for the LBM modeling of non-Newtonian fluid flows where viscosity may vary several orders of magnitude throughout the fluid domain, potentially causing variations of similar magnitude in the model numerical error. It turns out that, even when TRT or MRT models are used to ensure the proper parametrization of the LBM bulk solution with respect to viscosity, this property does not automatically extend to the boundary scheme closure relation [62, 63]. Consequently, the second purpose of this work is the LBM modeling of the non-Newtonian rheological condition and how it is handled by the LBM slip boundary scheme, either set in linear or

non-linear forms.

To model the slip velocity boundary condition, this work will make use of the local second order boundary (LSOB) method [67,68] that was recently revived in [37,69]. Our goal is to extend this boundary scheme to cope with a variety of wall slip laws, comprising the Navier linear [43], Navier non-linear [70], the empirical asymptotic [21] and Hatzikiriakos [71] slip laws. In the end, the prescription of any of these slip conditions will be approximated by our proposed LSOB scheme with a second-order accuracy on either straight or curved wall surfaces, either of which not necessarily conforming with the underlying LBM uniform mesh. On top of this requirement, the boundary scheme here developed will also be able to accommodate both Newtonian and non-Newtonian (Sisko) rheological fluid models, which brings in an additional modification of the original LSOB method. The formulations of these models will be exemplified for a microchannel flow as application case. For generality, they will be applied to both 2D and 3D microchannel geometries, considering both planar and curved walls.

The remaining manuscript will be organized as follows. Section 2 presents the LBM algorithm, with focus on the TRT collision model. Section 3 briefly revises the link between LBM and macroscopic variables in terms of Chapman-Enskog expansions [74]. Section 4 and Section 5 outline, respectively, the non-Newtonian rheological models and the slip laws considered in this work. Section 6 introduces the local second order boundary (LSOB) method and explains how the slip velocity condition and non-Newtonian fluid models are incorporated into the boundary scheme formulation. Section 7 provides the numerical evaluation of the proposed models by testing in Subsection 7.1 an horizontal channel, in Subsection 7.2 an inclined diagonal channel, and in Subsection 7.3 a circular tube geometry. Finally, Section 8 concludes the work with a summary of the main results. The manuscript is complemented with four appendix sections, where details on the derivation of key equations shown in the work are presented.

2 The lattice Boltzmann method

The LBM [22–24] solves for the populations $f_q(\boldsymbol{x},t)$ located at position $\boldsymbol{x}$ and time t along the discrete velocity $\boldsymbol{c}_q$. The discrete velocity set $\{\boldsymbol{c}_q : q=0,\cdots,Q-1\}$ considers one rest velocity $\boldsymbol{c}_0=\boldsymbol{0}$, and $Q-1$ non-zero velocities linking to neighboring nodes, which collectively form the lattice, where the streaming step takes place. The physical model is embedded into the collision step. Here, the two-relaxation-time (TRT) collision model [63–65] is adopted, which is formulated on the lattice symmetry argument that any lattice quantity ψ_q may be decomposed into symmetric ψ_q^+ and anti-symmetric ψ_q^- modes based on $\psi_q^\pm=\frac{1}{2}(\psi_q\pm\psi_{\bar{q}})$, where $\vec{c}_{\bar{q}}=-\vec{c}_q$.

The algorithm of the LBM-TRT scheme is structured along a succession of the following streaming and collision steps, where simulation units $\Delta x=\Delta t=1$ will be employed

hereinafter:

$$f_q(\boldsymbol{x}+\boldsymbol{c}_q,t+1)=\widehat{f}_q(\boldsymbol{x},t), \qquad q=0,1,\cdots,Q-1, \tag{2.1a}$$
$$\widehat{f}_q(\boldsymbol{x},t)=[f_q+\hat{n}_q^+ +\hat{n}_q^- +S_q^+ +S_q^-](\boldsymbol{x},t), \qquad q=0,1,\cdots,\tfrac{Q-1}{2}, \tag{2.1b}$$
$$\widehat{f}_{\bar{q}}(\boldsymbol{x},t)=[f_{\bar{q}}+\hat{n}_q^+ -\hat{n}_q^- +S_q^+ -S_q^-](\boldsymbol{x},t), \qquad q=1,\cdots,\tfrac{Q-1}{2}. \tag{2.1c}$$

In TRT terminology, the parameters $\widehat{f}_q$ denote the post-collision state of populations, $S_q^{\pm}$ are (symmetric/antisymmetric) source terms, and the post-collision non-equilibrium terms are defined as $\hat{n}_q^{\pm}=-n_q^{\pm}/\tau^{\pm}$, where $\tau^{\pm}$ are (symmetric/antisymmetric) relaxation times, and $n_q^{\pm}=f_q^{\pm}-e_q^{\pm}$ are (symmetric/antisymmetric) non-equilibrium populations, where $e_q^{\pm}$ are (symmetric/antisymmetric) equilibrium populations.

This work considers the simulation of incompressible slow viscous flows, which can be represented by the following linear (Stokes) equilibrium [62]:

$$e_q^+ = t_q P, \tag{2.2a}$$
$$e_q^- = t_q c_{q\alpha}\left(j_\alpha - \frac{1}{2}F_\alpha\right). \tag{2.2b}$$

Eq. (2.2a) introduces pressure P, which relates to fluid density ρ through the equation of state $P=c_s^2\rho$, with c_s^2 a free parameter subject to stability bounds [79], and Eq. (2.2b) introduces the fluid momentum $j_\alpha := \rho_0 u_\alpha$, where $\rho_0=$ const. [22–24] and u_α the fluid velocity. For notation simplicity, this work will consider $\rho_0=1$ (simulation units), meaning the terms fluid momentum and velocity will be used interchangeably while sticking with the j_α notation. Eq. (2.2b) also includes one half of the external body force F_α. This work reserves the use of Greek indices, such as index α, to denote the components of vector quantities. The external body force is contained within the $S_q^{\pm}$ source term [75–77] given by:

$$S_q^+ = 0, \tag{2.3a}$$
$$S_q^- = t_q c_{q\alpha} F_\alpha. \tag{2.3b}$$

Eqs. (2.2) and (2.3) adopt hydrodynamic weights t_q, which obey the required isotropic constraints $\sum_{q=1}^{Q-1} t_q c_{q\alpha} c_{q\beta}=\delta_{\alpha\beta}$ and $\sum_{q=1}^{Q-1} t_q c_{q\alpha} c_{q\beta} c_{q\gamma} c_{q\xi}=\frac{1}{3}\left(\delta_{\alpha\beta}\delta_{\gamma\xi}+\delta_{\alpha\gamma}\delta_{\beta\xi}+\delta_{\alpha\xi}\delta_{\beta\gamma}\right)$; for more details refer to [22–24]. The relation between the above denoted macroscopic fields and the mesoscopic populations f_q, solved by Eq. (2.1), are determined through the discrete velocity moments:

$$\rho=\sum_{q=0}^{Q-1} f_q, \quad j_\alpha=\sum_{q=1}^{Q-1} f_q c_{q\alpha}+\frac{1}{2}F_\alpha, \quad F_\alpha=\sum_{q=1}^{Q-1} S_q^- c_{q\alpha}. \tag{2.4}$$

The conservation laws satisfied by f_q are expressed by the mass and momentum constraints on the non-equilibrium components:

$$\sum_{q=0}^{Q-1} \hat{n}_q^+ = 0, \quad \sum_{q=1}^{Q-1} \hat{n}_q^- c_{q\alpha} = 0. \tag{2.5}$$

By unfolding the content of the non-equilibrium $\hat{n}_q^{\pm}$, via the standard Chapman-Enskog analysis – a task that will be detailed next in Section 3, see Eqs. (3.3) – it can be proven that, within a second-order level of approximation [37, 64, 69], the conservation statements provided by Eq. (2.5) lead to the Stokes flow equations in bulk:

$$\partial_\alpha j_\alpha = 0, \quad \partial_\alpha P - F_\alpha = \partial_\beta \left[\nu \left(\partial_\beta j_\alpha + \partial_\alpha j_\beta \right) \right], \quad \nu = \frac{\Lambda^+}{3}. \tag{2.6}$$

Due to the neglect of fluid inertia, the unsteady term $\partial_t j_\alpha$ is also omitted from the momentum balance in Eq. (2.6). In fact, as discussed by Happel and Brenner [72], the time variable is implicit in these equations. For the sake of application, this work will only consider time-independent flows. Furthermore, the fluid kinematic viscosity ν is allowed to vary in space, through a prescribed non-uniform Λ^+ value, as explained in Section 4, which covers the non-Newtonian models implementation. Note that $\Lambda^+ := \left(\tau^+ - \frac{1}{2}\right)$ and $\Lambda^- := \left(\tau^- - \frac{1}{2}\right)$ are the symmetric and anti-symmetric relaxation eigenfunctions of the TRT collision process, and their product defines the key collision relaxation parameter $\Lambda := \Lambda^+ \Lambda^-$, which controls the stationary field of non-dimensional TRT solutions [63] at all orders, i.e. beyond the second order hydrodynamic limit, given by Eq. (2.6). This work considers the $D2Q9$ and $D3Q19$ lattices to model 2D and 3D flows, respectively.

3 Chapman-Enskog steady-state approximations

The content of the non-equilibrium populations can be expressed in terms macroscopic quantities by using the Chapman-Enskog expansion [74]. This process unfolds the post-collision non-equilibrium populations, $\hat{n}_i^{\pm}$ through a perturbation parameter, ϵ, which is related to the ratio of the lattice unit to a characteristic length scale, $\epsilon \sim 1/h$, where $h := N\Delta x$ is a grid scale measure. Here, this expansion is developed, up to $\mathcal{O}(\epsilon^3)$, as follows: $\hat{n}_q^{\pm} = \epsilon \hat{n}_q^{(1)\pm} + \epsilon^2 \hat{n}_q^{(2)\pm} + \mathcal{O}(\epsilon^3)$. Based on Eqs. (A.2) of work [64], where $\partial_\alpha = \epsilon \partial_\alpha^{(1)}$ and $S_q^{\pm} = \epsilon S_q^{\pm(1)}$, together with the steady flow ($\partial_t = 0$) assumption, the explicit content of symmetric non-equilibrium populations $\hat{n}_q^{(1)+}$ and $\hat{n}_q^{(2)+}$ reads as follows:

$$\hat{n}_q^{+(1)} = c_{q\beta} \partial_\beta^{(1)} e_q^- - S_q^{+(1)}, \tag{3.1a}$$

$$\hat{n}_q^{+(2)} = -c_{q\alpha} c_{q\beta} \partial_\alpha^{(1)} (\Lambda^- \partial_\beta^{(1)} e_q^+). \tag{3.1b}$$

Conversely, the explicit content of anti-symmetric non-equilibrium populations $\hat{n}_q^{(1)-}$ and $\hat{n}_q^{(2)-}$ reads as follows:

$$\hat{n}_q^{-(1)} = c_{q\alpha}\partial_\alpha^{(1)} e_q^+ - S_q^{-(1)}, \tag{3.2a}$$

$$\hat{n}_q^{-(2)} = -c_{q\alpha}c_{q\beta}\partial_\alpha^{(1)}(\Lambda^+\partial_\beta^{(1)} e_q^-). \tag{3.2b}$$

Now, let us substitute the contents of Eq. (2.2) into $e_q^\pm$ and of Eq. (2.3) into $S_q^\pm$ and subsequently gather the ϵ and ϵ^2 terms back into $\hat{n}_q^\pm$. As a result, Eq. (3.1) and Eq. (3.2) reduce to [37, 67–69]:

$$\hat{n}_q^+ = t_q c_{q\alpha}c_{q\beta}\partial_\beta j_\alpha + \mathcal{O}(\epsilon^3) \tag{3.3a}$$

$$\hat{n}_q^- = -t_q c_{q\alpha}\left(3c_{q\beta}^2 - 1\right)\partial_\beta(\nu\partial_\beta j_\alpha) + \mathcal{O}(\epsilon^4). \tag{3.3b}$$

In the derivation of the above equations the following assumptions were undertaken. First, when deriving Eq. (3.3a) the term $\hat{n}_q^{+(2)}$ was discarded, based on the fact that $\partial_{\alpha\alpha}P=0$, as dictated by the Stokes flow assumption and the fact that for channel flow configurations the term $\partial_\beta\Lambda^-\partial_\alpha P$ reduces to $\partial_x\Lambda^-\partial_x P$, which owing to the fully-developed flow assumption leads to $\partial_x\Lambda^-=0$; otherwise, for more general flow configurations, this term can be transformed into $\partial_\beta\Lambda^-\left(F_\alpha-\partial_\beta\left(\nu\partial_\beta j_\alpha\right)\right)$ by invoking the bulk flow equation, where $\partial_\beta\Lambda^-$ and F_α are both known parameters, and $\partial_\beta\left(\nu\partial_\beta j_\alpha\right)$ is the only unknown. Second, when deriving Eq. (3.3b) the term $\hat{n}_q^{-(1)}$, which provides $\partial_\alpha P - F_\alpha$, was replaced by $\partial_\beta\left(\nu\partial_\beta j_\alpha\right)$ by invoking the bulk flow equation governing this problem, Eq. (2.6), similarly to the procedure taken for the $\hat{n}_q^{+(2)}$ simplification.

4 Non-Newtonian rheological models

Contrary to the Newtonian fluid framework, which by definition sets $\nu=$const., the rheological model of a non-Newtonian fluid allows viscosity to vary [45]. The non-Newtonian formulation considered in this work is the Sisko model [46], which is a generalization of the power-law model [47]. The Sisko model establishes a non-linear relationship between the kinematic viscosity and the local shear-rate as follows:

$$\nu(\dot{\gamma}) = \nu_\infty + a|2\dot{\gamma}|^{n-1}, \tag{4.1}$$

where $\dot{\gamma}=\frac{1}{2}\left(\partial_\alpha j_\beta+\partial_\beta j_\alpha\right)$ is the shear-rate, $a>0$ is a consistency index, $n\geq 0$ is the non-Newtonian exponent, and $\nu_\infty>0$ is the viscosity at very large shear-rates; for more details on these parameters, we refer to work [16]. As particular cases of Sisko model it can be inferred that $\nu_\infty=0$ recovers the power-law model, while setting $n=1$ retrieves the Newtonian rheological law.

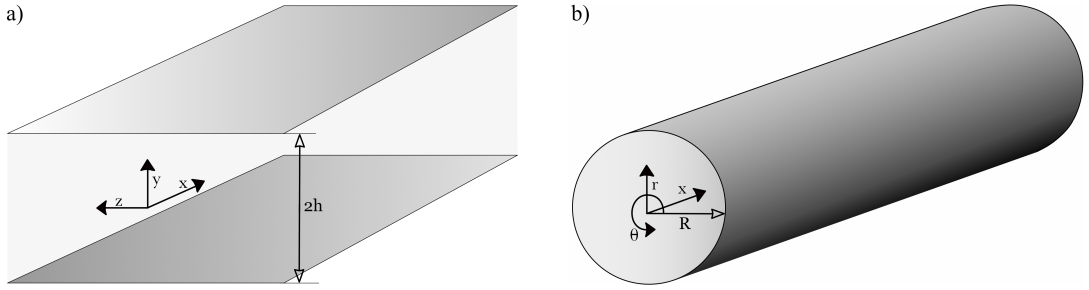

Figure 1: Geometrical configurations and related coordinate systems studied in this work. Panel (a): 2D planar channel. Panel (b): 3D Circular tube.

When applied to a straight, fully-developed flow in a 2D slit geometry, with momentum solution $\boldsymbol{j}=j_x(y)\boldsymbol{e_x}$, Eq. (4.1) reduces to:

$$\nu(y)=\nu_\infty+a|\partial_y j_x(y)|^{n-1}, \tag{4.2}$$

whereas for a fully-developed flow in a 3D circular tube, with momentum solution $\boldsymbol{j}=j_x(r)\boldsymbol{e_x}$, Eq. (4.1) leads to:

$$\nu(r)=\nu_\infty+a|\partial_r j_x(r)|^{n-1}. \tag{4.3}$$

Fig. 1 depicts these geometries and the associated coordinate systems. The mapping between the Cartesian and the cylindrical coordinates systems is summarized in Appendix A.

To determine the viscosity ν, the shear-rate components need to be computed. For this task, finite-differences (FD) could be applied over the velocity solution (e.g. using the solution from a previous iteration step). However, the use of FDs would break locality, an important asset of the LBM algorithm. To get around this shortcoming, we consider the well-known local relationship between the shear-rate and the LBM non-equilibrium populations [78, 80] (here represented in the TRT framework), which according to Eq. (3.3a) is explicitly given by:

$$\begin{aligned}\dot{\gamma}_{\alpha\beta}&=\frac{3}{2}\sum_{q=1}^{Q-1}\hat{n}_q^+c_{q\alpha}c_{q\beta}\\&=\frac{3}{2}\sum_{q=1}^{Q-1}t_q c_{q\alpha}c_{q\beta}c_{q\gamma}c_{q\delta}\partial_\xi j_\gamma+\mathcal{O}(\epsilon^3)\\&=\frac{3}{2}\partial_\xi j_\gamma\frac{1}{3}\left(\delta_{\alpha\beta}\delta_{\gamma\xi}+\delta_{\alpha\gamma}\delta_{\beta\xi}+\delta_{\alpha\xi}\delta_{\beta\gamma}\right)+\mathcal{O}(\epsilon^3)\\&=\frac{1}{2}\left(\partial_\alpha j_\beta+\partial_\beta j_\alpha\right)+\mathcal{O}(\epsilon^3).\end{aligned} \tag{4.4}$$

For planar and circular channel flows sufficiently far from inlet and outlet regions, the shear-rate tensor features one non-trivial component only, given by $\dot{\gamma}_{xy}(\boldsymbol{x})=$

$\frac{1}{2}\left(\partial_y j_x(\boldsymbol{x})+\cancel{\partial_x j_y(\boldsymbol{x})}\right)$ and $\dot{\gamma}_{xr}(\boldsymbol{x})=\frac{1}{2}\left(\partial_r j_x(\boldsymbol{x})+\cancel{\partial_x j_r(\boldsymbol{x})}\right)$, respectively. After the determination of $\dot{\gamma}$, through Eq. (4.4), the local assessment of the kinematic viscosity ν follows directly from Eq. (4.1). When it comes down to the numerical computation of ν in this way, we note that the under-relaxation of the kinematic viscosity computation is sometimes necessary to achieve converged steady-state solutions; this stability issue is particularly stringent when $n<1$, rendering the LBM modeling of fluids with shear-thinning behavior more challenging than those with shear-thickening characteristics.

Remark 4.1. In the LBM-TRT modelling of non-Newtonian fluids, the local variation of Λ^+ must be balanced by Λ^-, as $\Lambda^-=\Lambda/\Lambda^+$, such that Λ holds constant throughout the domain. The constancy of Λ is the necessary condition to ensure that the numerical error of the LBM steady-state solution remains unaffected by the viscosity local value [63–65]. Otherwise, the implementation of non-Newtonian rheological models within a single relaxation time framework, such as BGK [81], will inevitably violate this requirement, since $\Lambda=9\nu^2$ in the BGK model. Consequently, the non-linear ν-dependence on the numerical errors renders the LBM-BGK scheme an inconsistent numerical model for non-Newtonian fluid flows, since it does not guarantee that the solution parametrization is exclusively controlled by the relevant dimensionless groups of the physical problem, as presented in Section 7.

5 Slip velocity boundary condition models

Consider a time-independent fluid flow bounded by rigid, solid and resting walls. At the wall location, $\boldsymbol{x}_{\rm w}$, the wall-normal velocity component $(\boldsymbol{j}\cdot\boldsymbol{n})\big|_{\boldsymbol{x}_w}=0$ is subject to the impermeability condition and the wall tangential velocity component $(\boldsymbol{j}\cdot\boldsymbol{s})\big|_{\boldsymbol{x}_w}=j_{\rm ws}$ is subject to a slip velocity boundary condition. As slip condition, this study considers the linear slip model and three non-linear slip laws. They are all formulated on the wall-aligned coordinate system, where n is the outward unitary wall normal vector and s is the unitary wall tangential vector parallel to the main flow direction. For the planar and circular channels, depicted in Fig. 1, this coordinate system takes the following form: (i) planar channel $(s,n)\mapsto(x,\pm y)$ (where the $+/-$ sign refers to bottom/top walls, respectively) and (ii) circular tube $(s,n)\mapsto(x,-r)$.

The Navier linear (NL) slip velocity model [43] prescribes the fluid velocity at the wall, $j_{\rm ws}$, as follows:

$$j_{\rm ws}=\mathrm{sgn}(\partial_n j_s)\,k_l\,(\tau_{ns})\big|_{\boldsymbol{x}_w}, \tag{5.1}$$

where $k_l\geq 0$ is a prescribed slip coefficient.

The Navier non-linear (NNL) slip velocity model [70] generalizes NL slip model as follows:

$$j_{\rm ws}=\mathrm{sgn}(\partial_n j_s)\,k_{nl}\left(|\tau_{ns}|^{m-1}\tau_{ns}\right)\big|_{\boldsymbol{x}_w}, \tag{5.2}$$

where $k_{nl} \geq 0$ is a prescribed slip coefficient and $m > 0$. For $m = 1$ the classical Navier linear slip model is recovered.

The asymptotic (ASP) slip velocity model [21] is described as follows:

$$j_{\text{ws}} = k_{a_1} \ln\left(1 + k_{a_2} \operatorname{sgn}(\partial_n j_s)\, \tau_{ns}\right)\Big|_{\boldsymbol{x}_w}, \tag{5.3}$$

where $k_{a_1} \geq 0$ and $k_{a_2} \geq 0$ are prescribed slip parameters.

The Hatzikiriakos (HZK) slip velocity model [71] is formulated as follows

$$j_{\text{ws}} = \begin{cases} k_{h_1} \sinh\left(k_{h_2} \operatorname{sgn}(\partial_n j_s)\,(\tau_{ns} - \tau_c)\right)\Big|_{\boldsymbol{x}_w}, & \text{if } \tau_{ns} \geq \tau_c, \\ 0, & \text{otherwise,} \end{cases} \tag{5.4}$$

where τ_c is a positive critical stress which denotes the onset of slip, and $k_{h_1} \geq 0$ and $k_{h_2} \geq 0$ are prescribed slip parameters.

The wall shear stress $\tau_{ns}(\boldsymbol{x}_w)$ in all above slip laws is determined by:

$$\tau_{ns}(\boldsymbol{x}_w) = \nu(\boldsymbol{x}_w)\, \partial_n j_s(\boldsymbol{x}_w), \tag{5.5}$$

where $\nu(\boldsymbol{x}_w)$ and $\partial_n j_s(\boldsymbol{x}_{\text{w}})$ are computed locally, as was explained in Section 4.

6 Local second order boundary (LSOB) method

The physical slip boundary conditions, presented in Section 5, are prescribed in the LBM model through the local second order boundary (LSOB) method [37, 67–69]. The idea behind LSOB relies on the explicit reconstruction of the unknown boundary populations, based on the exact decomposition of TRT populations:

$$f_q(\boldsymbol{x},t) = \left[e_q^+ + e_q^- - \tau^+ \hat{n}_q^+ - \tau^- \hat{n}_q^-\right](\boldsymbol{x},t). \tag{6.1}$$

The equilibrium components e_q^+ and e_q^- are set by Eqs. (2.2a) and (2.2b), respectively. The non-equilibrium components $\hat{n}_q^+$ and $\hat{n}_q^-$ can be approximated by using Eqs. (3.3a) and (3.3b), respectively. The relaxation rates τ^+ and τ^- vary locally, where τ^+ is related to the fluid viscosity ν, according to the Sisko model, given by Eq.(4.1), and $\tau^- = \frac{1}{2} + \frac{\Lambda}{(\tau^+ - \frac{1}{2})}$. The LSOB applies Eq. (6.1) to the unknown boundary populations only, i.e. those that propagate from the boundary node $\boldsymbol{x}_b$ towards inside the fluid domain. To proceed further and unfold the explicit content of each term in Eq. (6.1) one requires the knowledge of the flow and the bounding geometry. This task will be exemplified next for a 2D planar channel and a 3D circular tube.

6.1 LSOB for a 2D horizontal planar channel

Consider a 2D planar channel that contains a non-Newtonian fluid obeying Sisko model. Starting from Eqs. (3.3a) and (3.3b), the $\hat{n}_q^+$ and $\hat{n}_q^-$ non-equilibrium populations in this case can be explicitly written as:

$$\hat{n}_q^+ = t_q c_{qx} c_{qy} \partial_y j_x, \tag{6.2a}$$

$$\hat{n}_q^- = -t_q c_{qx} \left(3c_{qy}^2 - 1\right) \left[(n-1)(\nu - \nu_\infty) + \nu\right] \partial_{yy} j_x. \tag{6.2b}$$

The derivation of Eq. (6.2b) is detailed in Appendix B. The consideration of the non-Newtonian viscosity law only affects the $\hat{n}_q^-$ formulation through the coefficient $[(n-1)(\nu-\nu_\infty)+\nu]$.

Eq. (6.2) can be cast in matrix form to determine the momentum derivative terms.

$$\underbrace{\begin{bmatrix} \hat{n}_q^+(\boldsymbol{x}_b) \\ \hat{n}_q^-(\boldsymbol{x}_b) \end{bmatrix}}_{\mathcal{N}} = \underbrace{\begin{bmatrix} t_q c_{qx} c_{qy} & 0 \\ 0 & -t_q c_{qx} \left(3c_{qy}^2 - 1\right) \overline{\nu} \end{bmatrix}}_{[\mathbf{M}]} \underbrace{\begin{bmatrix} \partial_y j_x(\boldsymbol{x}_b) \\ \partial_{yy} j_x(\boldsymbol{x}_b) \end{bmatrix}}_{\mathcal{X}}, \tag{6.3}$$

where $\overline{\nu} = [(n-1)(\nu-\nu_\infty)+\nu]$. In the system above $\mathcal{N}$ is a vector formed by the known populations, the matrix $[\mathbf{M}]$ is formed by the coefficients of the LSOB approximations, and $\mathcal{X}$ is the vector formed by the unknown momentum derivatives at $\boldsymbol{x}_b$. Based on this representation, the content of $\mathcal{X}$ is locally available through the solution of the following linear algebra problem:

$$\mathcal{X} = [\mathbf{M}]^{-1} \mathcal{N}. \tag{6.4}$$

Due to the shear-rate viscosity dependence, the solution of Eq. (6.4) must be computed at each iteration step to update $\overline{\nu}$. Although it is straightforward to compute $[\mathbf{M}]^{-1}$, its solution may become unstable when $\overline{\nu}$ becomes too large (although, at this stage, our criterion of "too large" is solely based on heuristic arguments owing to the current lack of more rigorous stability analyses for LBM boundary schemes [89]). Nonetheless, numerical experiments run on a wide range of non-Newtonian viscosity parameters reveal that stability can be guaranteed providing the coefficients in $[\mathbf{M}]^{-1}$ are kept bounded to small values throughout consecutive iterations. In order to fulfill this requirement we employ a typical under-relaxation procedure during the determination of the momentum derivatives in $\mathcal{X}$, which are then used to construct the $\overline{\nu}$ term. By following this procedure, we could always reach a stable and unique solution, although at the cost of increasing the total number of iteration steps to reach the steady-state convergence. Alternatives to this stabilization procedure will be explored in future studies; in this context, a strong candidate could be the use of LBM steady-state solvers [79], which bypass the transient stage of the computation, where typically these numerical instabilities arise and get amplified.

After finding the content of $\mathcal{X}$, it is possible to explicitly reconstruct the incoming boundary populations, at $\boldsymbol{x}_b$, as follows:

$$f_q(\boldsymbol{x}_b) = t_q P(\boldsymbol{x}_b) + t_q c_{qx} \left[j_x(\boldsymbol{x}_b) - \frac{1}{2} F_x - \tau^+(\boldsymbol{x}_b) c_{qy} \partial_y j_x(\boldsymbol{x}_b) \right.$$
$$\left. + \tau^-(\boldsymbol{x}_b) \left(3c_{qy}^2 - 1\right) \left[(n-1)(\nu - \nu_\infty) + \nu\right] \partial_{yy} j_x(\boldsymbol{x}_b) \right], \tag{6.5}$$

where $\nu = \nu(\boldsymbol{x}_b)$. To complete the reconstruction of $f_q(\boldsymbol{x}_b)$ in Eq. (6.5), two hydrodynamic quantities must be determined: $P(\boldsymbol{x}_b)$ and $j_x(\boldsymbol{x}_b)$.

First, the boundary pressure value $P(\boldsymbol{x}_b)$ is obtained via the zeroth-order mass moment, which is split into known $\mathcal{K}$ and unknown $\mathcal{U}$ sets. The result is given by: $\frac{P}{c_s^2} = \sum_{q\in\mathcal{K}} f_q + \sum_{q\in\mathcal{U}} f_q$, where the part of f_q belonging to the $\mathcal{U}$ set is subject to the LSOB approximation. On this basis, $P(\boldsymbol{x}_b)$ is computed as follows:

$$P(\boldsymbol{x}_b) = \frac{1}{c_s^{-2} - \sum_{q\in\mathcal{U}} t_q} \left[\sum_{q\in\mathcal{K}} f_q(\boldsymbol{x}_b) + \left(j_x(\boldsymbol{x}_b) - \tfrac{1}{2} F_x\right) \sum_{q\in\mathcal{U}} t_q c_{qx} - \tau^+(\boldsymbol{x}_b) \sum_{q\in\mathcal{U}} \hat{n}_q^+(\boldsymbol{x}_b) \right.$$
$$\left. - \tau^-(\boldsymbol{x}_b) \sum_{q\in\mathcal{U}} \hat{n}_q^-(\boldsymbol{x}_b) \right], \tag{6.6}$$

where $j_x(\boldsymbol{x}_b)$ is computed as explained next.

Second, the boundary node momentum value $j_x(\boldsymbol{x}_b)$ is obtained by relating it with respect to the prescribed wall boundary condition, considered in Section 5. The relation between the fluid momentum at the wall $j_x(\boldsymbol{x}_w)$ and its boundary node value $j_x(\boldsymbol{x}_b)$ is established via the second-order Taylor series approximation:

$$j_x(\boldsymbol{x}_b) = j_x(\boldsymbol{x}_w) + \delta_y \partial_y j_x(\boldsymbol{x}_b) - \frac{\delta_y^2}{2} \partial_{yy} j_x(\boldsymbol{x}_b), \tag{6.7}$$

where the distance between wall and boundary node is:

$$\delta_y = (\boldsymbol{x}_b - \boldsymbol{x}_w) \cdot \boldsymbol{e}_y \tag{6.8}$$

with $\boldsymbol{e}_y$ the vertical unit vector (aligned with wall normal vector) of the (x,y,z) system, see Fig. 1. In Eq. (6.7) the momentum derivatives $\partial_y j_x(\boldsymbol{x}_b)$ and $\partial_{yy} j_x(\boldsymbol{x}_b)$ are provided by Eq. (6.4), applied to Eq. (6.3), whereas the fluid momentum at the wall, $j_x(\boldsymbol{x}_w)$, is determined by the physical boundary condition of the problem. For the slip models presented in Section 5, the $j_x(\boldsymbol{x}_w)$ may be given by Eq. (5.1) for NL, Eq. (5.2) for NNL, Eq. (5.3) for ASP, or Eq. (5.4) for HZK slip models. Here, to account for the planar wall geometry, the wall shear stress is mapped onto Cartesian coordinates, $\tau_{ns} \mapsto \tau_{xy}$, so that:

$$\tau_{xy}(\boldsymbol{x}_w) = \nu(\boldsymbol{x}_w) \partial_y j_x(\boldsymbol{x}_w). \tag{6.9}$$

As the derivative $\partial_y j_x(\boldsymbol{x}_w)$ is also unknown, it is once again approximated as a second-order Taylor series, where the relation between wall and boundary node derivatives is expressed as:

$$\partial_y j_x(\boldsymbol{x}_w) = \partial_y j_x(\boldsymbol{x}_b) - \delta_y \partial_{yy} j_x(\boldsymbol{x}_b). \tag{6.10}$$

The viscosity $\nu(\boldsymbol{x}_w)$ in Eq. (6.9) is given by Eq. (4.2), and is again determined with the help of Eq. (6.10) to determine $\partial_y j_x(\boldsymbol{x}_w)$. This exposition concludes the reconstruction of $f_q(\boldsymbol{x}_b)$, as given by Eq. (6.5), which incorporates the slip velocity model, given in Section 5, and the non-Newtonian viscosity law, given in Section 4.

Similarly to the non-Newtonian fluid flow modeling, also the modeling of the slip velocity condition within the LSOB framework may pose specific stability challenges in the reconstruction of $f_q(\boldsymbol{x}_b)$, given by Eq. (6.5). During the LBM iterative process, the boundary node momentum derivatives used in the reconstruction of $f_q(\boldsymbol{x}_b)$ may become unwieldy sharp, particularly under large slip conditions. This issue is even more damaging when dealing with non-linear slip laws as these sharp momentum derivatives get non-linearly amplified. In order to prevent the solution blow-up, we followed the same strategy used to stabilize the non-Newtonian rheology model and employed an under-relaxation procedure in the determination of the momentum derivatives in $\mathcal{X} = [\mathbf{M}]^{-1}\mathcal{N}$. While this procedure leads to a slight increase in the number of iterations, it guarantees stable steady-state solutions over a wide range of slip regimes.

The workflow of the LSOB algorithm, described above, can be summarized as follows:

1. Construct and update the matrix $[\mathbf{M}]$ at each iteration.
2. Select relevant $\hat{n}_q^{\pm}$ populations and assemble vector $\mathcal{N}$ after each collision step.
3. Compute $\mathcal{X} = \{\partial_y j_x(\boldsymbol{x}_b), \partial_{yy} j_x(\boldsymbol{x}_b)\}$ from the linear algebra problem $\mathcal{X} = [\mathbf{M}]^{-1}\mathcal{N}$, given by Eq. (6.3).
4. Determine $\partial_y j_x(\boldsymbol{x}_w)$ based on Eq. (6.10).
5. Determine $\nu(\boldsymbol{x}_w)$ based on Eq. (4.2), using $\partial_y j_x(\boldsymbol{x}_w)$ from Eq. (6.10).
6. Determine $\tau_{xy}(\boldsymbol{x}_w)$ based on Eq. (6.9).
7. Determine $j_x(\boldsymbol{x}_w)$ based on the selected slip boundary model, e.g., Eq. (5.2) for NNL, Eq. (5.3) for ASP, or Eq. (5.4) for HZK slip models, with $\tau_{xy}(\boldsymbol{x}_w)$ then given by Eq. (6.9).
8. Compute $j_x(\boldsymbol{x}_b)$ based on Eq. (6.7), using $j_x(\boldsymbol{x}_w)$ and $\mathcal{X} = \{\partial_y j_x(\boldsymbol{x}_b), \partial_{yy} j_x(\boldsymbol{x}_b)\}$, to be used in Eq. (6.5).
9. Compute $P(\boldsymbol{x}_b)$ based on Eq. (6.6), to be used in Eq. (6.5).
10. Construct unknown $f_q(\boldsymbol{x}_b)$ populations according to Eq. (6.5) using $j_x(\boldsymbol{x}_b)$ and $P(\boldsymbol{x}_b)$ previously computed in steps 8 and 9.

Remark 6.1. According to the terminology used in previous works on the LSOB scheme [37, 69], the algorithm here presented may be referred to as the Lnode formulation. The other formulation that may be followed in the LSOB framework is the Lwall, which is easily derived from the Lnode case, by following the derivations displayed in works [37, 69]; therefore, its presentation is omitted herein.

6.2 LSOB for a 2D inclined planar channel

In this section, the 2D planar channel considered in Section 6.1 is extended for an inclined setup as sketched in Fig. 2. This geometry can be considered as a building block of more general configurations such as zig-zag like channels.

Consider a non-Newtonian Sisko-law fluid, which flows inside a 2D inclined planar channel (the Newtonian fluid flow derivation of this case was originally proposed in [67]). Starting from Eqs. (3.3a) and (3.3b), the $\hat{n}_q^+$ and $\hat{n}_q^-$ non-equilibrium populations

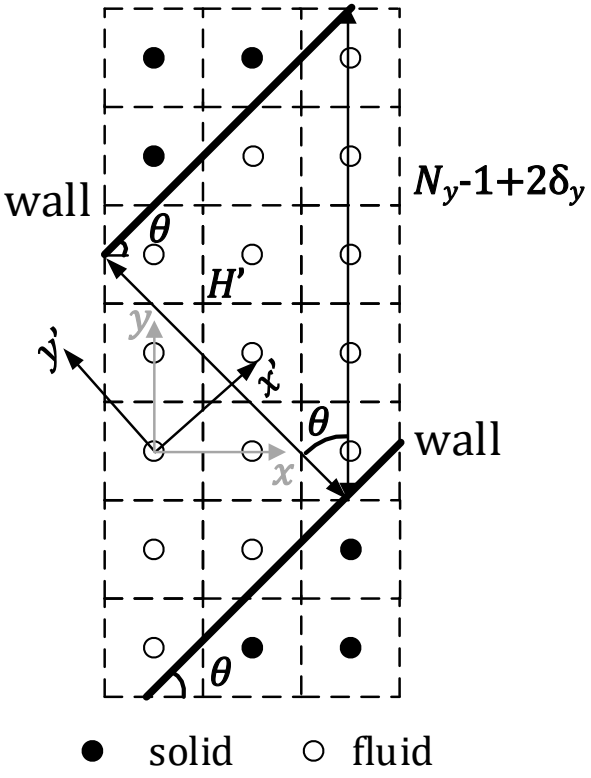

Figure 2: Discretization of 2D planar channel on the LBM uniform mesh. The streamline-rotated coordinate system (x',y') is aligned with the channel walls and rotated at an angle θ.

can be projected onto the streamline-rotated coordinate system (x',y'), rotated at an angle θ, which locally aligns with the channel walls [67]. The $\hat{n}_q^+$ and $\hat{n}_q^-$ content is given as follows:

$$\begin{aligned}\hat{n}_q^+ =& t_q\left(\frac{1}{2}\sin 2\theta\left(-c_{qx}^2+c_{qy}^2\right)+\cos 2\theta c_{qx}c_{qy}\right)\partial_{y'}j_{x'}\\ =& t_q c_{qx'}c_{qy'}\partial_{y'}j_{x'},\end{aligned} \tag{6.11a}$$

$$\begin{aligned}\hat{n}_q^- =& -t_q\left[\left(3c_{qy}^2-1\right)c_{qx}\cos\theta\left(\cos^2\theta-2\sin^2\theta\right)\right.\\ &\left.+\left(3c_{qx}^2-1\right)c_{qy}\sin\theta\left(\sin^2\theta-2\cos^2\theta\right)\right]\left[(n-1)(\nu-\nu_\infty)+\nu\right]\partial_{y'y'}j_{x'},\end{aligned} \tag{6.11b}$$

where $c_{qx'}=c_{qx}\cos\theta+c_{qy}\sin\theta$ and $c_{qy'}=-c_{qx}\sin\theta+c_{qy}\cos\theta$. Note that, unlike the second order term where the equality $c_{qx}c_{qy}\partial_y j_x = c_{qx'}c_{qy'}\partial_{y'}j_{x'}$ holds, the third order term is, in general, not invariant under an arbitrary space isometry [67], meaning $(3c_{qy}^2-1)c_x\partial_{yy}j_x \neq (3c_{qy'}^2-1)c_{x'}\partial_{y'y'}j_{x'}$, as shown in Eq. (6.11b). The derivation of Eq. (6.11b) is detailed in Appendix C. The consideration of the non-Newtonian viscosity law only affects the $\hat{n}_q^-$ formulation through the coefficient $[(n-1)(\nu-\nu_\infty)+\nu]$. In fact, the structure of the linear algebra problem $\mathcal{N}=[\mathbf{M}]\mathcal{X}$, which arises from this case, is quite similar to the horizontal channel setup, displayed in Eq. (6.3), with the only difference being in the $[\mathbf{M}]$ matrix elements.

In the end, after determining the content of $\mathcal{X}$, one is able to explicitly reconstruct the incoming boundary populations, at $\boldsymbol{x}_b$, for the inclined channel setup [67]:

$$\begin{aligned}f_q(\boldsymbol{x}_b) =& t_q P(\boldsymbol{x}_b)+t_q c_{qx'}\left[j_{x'}(\boldsymbol{x}_b)-\frac{1}{2}F_{x'}\right]-\tau^+(\boldsymbol{x}_b)c_{qx'}c_{qy'}\partial_{y'}j_{x'}(\boldsymbol{x}_b)\\ &+\tau^-(\boldsymbol{x}_b)\left[\left(3c_{qy}^2-1\right)c_{qx}\cos\theta\left(\cos^2\theta-2\sin^2\theta\right)\right.\\ &\left.+\left(3c_{qx}^2-1\right)c_{qy}\sin\theta\left(\sin^2\theta-2\cos^2\theta\right)\right]\left[(n-1)(\nu-\nu_\infty)+\nu\right]\partial_{y'y'}j_{x'}(\boldsymbol{x}_b).\end{aligned} \tag{6.12}$$

The two hydrodynamic quantities left to determine in Eq. (6.12) are $P(\boldsymbol{x}_b)$ and $j_x(\boldsymbol{x}_b)$. The boundary node pressure $P(\boldsymbol{x}_b)$ is also computed through Eq. (6.6), whereas the boundary node fluid momentum $j_{x'}(\boldsymbol{x}_b)$ is related to the wall fluid momentum according to Eq. (6.7), although the Taylor expansion is developed on the streamline-rotated coordinate system (x',y'), which reads:

$$j_{x'}(\boldsymbol{x}_b)=j_{x'}(\boldsymbol{x}_w)+\delta_{y'}\partial_{y'}j_{x'}(\boldsymbol{x}_b)-\frac{\delta_{y'}^2}{2}\partial_{y'y'}j_{x'}(\boldsymbol{x}_b), \tag{6.13}$$

where the distance between wall and boundary node on this rotated (x',y') reference frame is given by:

$$\delta_{y'}=(\boldsymbol{x}_b-\boldsymbol{x}_w)\cdot\boldsymbol{e}_{y'} \tag{6.14}$$

with $\boldsymbol{e}_{y'}$ being the vertical unit vector (aligned with wall normal vector) of the rotated system (x',y'); more details about the relations between fixed and rotated frames are presented in Appendix A.1.

The fluid momentum at the wall $j_{x'}(\boldsymbol{x}_w)$ in Eq. (6.13) is determined by the chosen slip boundary model that, according to Section 5, may follow Eq. (5.1) for NL, Eq. (5.2) for NNL, Eq. (5.3) for ASP, or Eq. (5.4) for HZK slip models. The main difference compared with the horizontal channel case is that the closure relation of these models must be expressed on the streamline-rotated coordinate system (x',y'). It is important to bear in mind that, in order to deal with any of the aforementioned wall slip models, we only make use of the known quantities $\partial_{y'}j_{x'}(\boldsymbol{x}_b)$ and $\partial_{y'y'}j_{x'}(\boldsymbol{x}_b)$, and therefore employ the inclined channel equivalents of Eq. (6.9) given by $\tau_{x'y'}(\boldsymbol{x}_w)=\nu(\boldsymbol{x}_w)\partial_{y'}j_{x'}(\boldsymbol{x}_w)$ and of Eq. (6.10) given by $\partial_{y'}j_{x'}(\boldsymbol{x}_w)=\partial_{y'}j_{x'}(\boldsymbol{x}_b)-\delta_{y'}\partial_{y'y'}j_{x'}(\boldsymbol{x}_b)$. Overall, the LSOB algorithm to prescribe the velocity slip condition in this case follows the same steps presented in Section 6.1.

6.3 LSOB for a 3D straight circular tube

For a 3D circular tube containing a non-Newtonian fluid obeying Sisko model, the $\hat{n}_q^+$ and $\hat{n}_q^-$ non-equilibrium populations can be explicitly written as:

$$\hat{n}_q^+ = t_q c_{qx}\left(c_{qy}\partial_y j_x + c_{qz}\partial_z j_x\right), \tag{6.15a}$$

$$\begin{aligned}\hat{n}_q^- =& -t_q c_{qx}\left[(n-1)(\nu-\nu_\infty)+\nu\right]\left[\left(3c_{qy}^2-1\right)\partial_{yy}j_x+\left(3c_{qz}^2-1\right)\partial_{zz}j_x\right]\\ &+t_q c_{qx}(n-1)(\nu-\nu_\infty)\left[\left(3c_{qy}^2-1\right)\sin^2\theta+\left(3c_{qz}^2-1\right)\cos^2\theta\right]\frac{1}{r}\left(\cos\theta\partial_y j_x+\sin\theta\partial_z j_x\right),\end{aligned} \tag{6.15b}$$

with $r=\sqrt{(y_b-y_0)^2+(z_b-z_0)^2}$ and (y_0,z_0) the origin of the coordinate axis. The derivation of Eq. (6.15b) is detailed in Appendix D.

Eq. (6.15) can be cast in matrix form to determine the momentum derivative terms as follows:

$$\underbrace{\begin{bmatrix}\hat{n}_q^+(\boldsymbol{x}_b)\\ \hat{n}_q^-(\boldsymbol{x}_b)\end{bmatrix}}_{\mathcal{N}} = \underbrace{\begin{bmatrix} t_q c_{qx}c_{qy} & t_q c_{qx}c_{qz} & 0 & 0\\ t_q c_{qx}\Phi_q\cos\theta\,(\overline{\nu}-\nu) & t_q c_{qx}\Phi_q\sin\theta\,(\overline{\nu}-\nu) & -t_q c_{qx}\left(3c_{qy}^2-1\right)\overline{\nu} & -t_q c_{qx}\left(3c_{qz}^2-1\right)\overline{\nu}\end{bmatrix}}_{[\mathbf{M}]}\underbrace{\begin{bmatrix}\partial_y j_x(\boldsymbol{x}_b)\\ \partial_z j_x(\boldsymbol{x}_b)\\ \partial_{yy}j_x(\boldsymbol{x}_b)\\ \partial_{zz}j_x(\boldsymbol{x}_b)\end{bmatrix}}_{\mathcal{X}}, \tag{6.16}$$

where $\overline{\nu}:=\left[(n-1)(\nu-\nu_\infty)+\nu\right]$ (recall $\nu=\nu(\boldsymbol{x}_b)$) and $\Phi_q:=\left[(3c_{qy}^2-1)\sin^2\theta+(3c_{qz}^2-1)\cos^2\theta\right]\frac{1}{r}$.

Above, $\mathcal{N}$ is a vector formed by the known populations, the matrix $[\mathbf{M}]$ is formed by the coefficients of the LSOB approximations, and $\mathcal{X}$ is the vector formed by the unknown momentum derivatives at $\boldsymbol{x}_b$. As in the 2D planar case, the content of $\mathcal{X}$ in this 3D problem is locally determined through the solution of a linear algebra system given by Eq. (6.4). However, unlike the 2D planar case previously presented, the 3D circular tube geometry leads to a non-trivial discretization procedure. Here, we are required to count the number of independent equations available, given by the number of linearly independent known populations at each boundary node, i.e. rank$[\mathbf{M}]$, and compare this number against the number of unknowns that must be determined inside $\mathcal{X}$, i.e. $\dim(\mathcal{X})$. If rank$[\mathbf{M}] \geq \dim(\mathcal{X})$ then the above linear algebra system is determined and Eq. (6.16) can be used directly to extract $\mathcal{X}$; we call these sites as *regular boundary nodes*. Otherwise, if rank$[\mathbf{M}] < \dim(\mathcal{X})$ the above linear algebra system is under-determined and we call these sites as *singular boundary nodes*. To guarantee their determinacy, the system must be augmented by additional conditions. Following previous works [37,69], we propose including the derivatives of the known wall tangent momentum condition along the boundary as the required supplementary conditions. For a curved wall surface, they read $\partial_\theta(j_x(\boldsymbol{x}_w)-j_{\rm ws})=0$ and $\partial_{\theta\theta}(j_x(\boldsymbol{x}_w)-j_{\rm ws})=0$, where $j_{\rm ws}$ is determined by the chosen slip velocity model; explicitly, $j_{\rm ws}$ is given by Eq. (5.1) for NL, Eq. (5.2) for NNL, Eq. (5.3) for ASP, or Eq. (5.4) for HZK slip models. Recall that, to account for the circular wall geometry, in all these slip models the wall shear stress is mapped onto cylindrical coordinates, $\tau_{ns} \mapsto \tau_{rx}$. The transcription of these conditions from $\boldsymbol{x}_w$ to $\boldsymbol{x}_b$ makes use of the second-order Taylor series approximation on the $j_x(\boldsymbol{x}_w)$ term and leads to:

$$\begin{cases} \partial_\theta(j_x(\boldsymbol{x}_w)-j_{\rm ws}) = (r-\delta_r)\left(-\sin\theta\partial_y j_x(\boldsymbol{x}_b)+\cos\theta\partial_z j_x(\boldsymbol{x}_b)\right) \\ \qquad\qquad +\delta_r r\left(\dfrac{1}{2}\sin 2\theta\left(\partial_{yy}j_x(\boldsymbol{x}_b)-\partial_{zz}j_x(\boldsymbol{x}_b)\right)-\cos 2\theta\partial_{yz}j_x(\boldsymbol{x}_b)\right)-\partial_\theta j_{\rm ws}=0, \\ \partial_{\theta\theta}(j_x(\boldsymbol{x}_w)-j_{\rm ws}) = -r\left(\cos\theta\partial_y j_x(\boldsymbol{x}_b)+\sin\theta\partial_z j_x(\boldsymbol{x}_b)\right) \\ \qquad\qquad +r^2\left(\sin^2\theta\partial_{yy}j_x(\boldsymbol{x}_b)+\cos^2\theta\partial_{zz}j_x(\boldsymbol{x}_b)-\sin 2\theta\partial_{yz}j_x(\boldsymbol{x}_b)\right)-\partial_{\theta\theta}j_{\rm ws}=0. \end{cases} \tag{6.17}$$

The last term in each equation, $\partial_\theta j_{\rm ws}$ and $\partial_{\theta\theta} j_{\rm ws}$, does not contain unknowns that need to be computed in the LSOB system. Rather, they are computed at each time step by using the information from the previous time step. How these two terms are computed for the various slip laws is presented in Appendix E.

We note that the distinction between regular and singular boundary nodes is only relevant during the linear algebra formulation problem, Eq. (6.4), which provides the boundary node momentum derivatives in $\mathcal{X}$. After the content of $\mathcal{X}$ is found the procedure is identical for all boundary nodes and the incoming boundary populations, at $\boldsymbol{x}_b$, are explicitly reconstructed as follows:

$$f_q(\boldsymbol{x}_b) = t_q P(\boldsymbol{x}_b) + t_q c_{qx}\left(j_x(\boldsymbol{x}_b)-\frac{1}{2}F_x\right)$$

$$
\begin{aligned}
&-t_q c_{qx}\left[\tau^+(\boldsymbol{x}_b)c_{qy}+\tau^-(\boldsymbol{x}_b)(\bar{\nu}-\nu)\left(\left(3c_{qy}^2-1\right)\sin^2\theta+\left(3c_{qz}^2-1\right)\cos^2\theta\right)\frac{\cos\theta}{r}\right]\partial_y j_x(\boldsymbol{x}_b)\\
&-t_q c_{qx}\left[\tau^+(\boldsymbol{x}_b)c_{qz}+\tau^-(\boldsymbol{x}_b)(\bar{\nu}-\nu)\left(\left(3c_{qy}^2-1\right)\sin^2\theta+\left(3c_{qz}^2-1\right)\cos^2\theta\right)\frac{\sin\theta}{r}\right]\partial_z j_x(\boldsymbol{x}_b)\\
&+t_q c_{qx}\left[\tau^-(\boldsymbol{x}_b)\left(3c_{qy}^2-1\right)\bar{\nu}\right]\partial_{yy} j_x(\boldsymbol{x}_b)\\
&+t_q c_{qx}\left[\tau^-(\boldsymbol{x}_b)\left(3c_{qz}^2-1\right)\bar{\nu}\right]\partial_{zz} j_x(\boldsymbol{x}_b).
\end{aligned}
\tag{6.18}
$$

The complete reconstruction of $f_q(\boldsymbol{x}_b)$ in Eq. (6.18) still requires the determination of $P(\boldsymbol{x}_b)$ and $j_x(\boldsymbol{x}_b)$. The boundary node pressure $P(\boldsymbol{x}_b)$ is calculated, as in the 2D planar wall case, according to Eq. (6.6). Likewise, the boundary node momentum value $j_x(\boldsymbol{x}_b)$ can also be computed by relating it to the prescribed boundary condition at $\boldsymbol{x}_b$ through the second-order Taylor series approximation:

$$
\begin{aligned}
j_x(\boldsymbol{x}_b) =& j_x(\boldsymbol{x}_w)+\delta_r\partial_r j_x(\boldsymbol{x}_b)-\frac{\delta_r^2}{2}\partial_{rr} j_x(\boldsymbol{x}_b)\\
=& j_x(\boldsymbol{x}_w)+\delta_r\left(1+\frac{\delta_r}{2r}\right)\left(\cos\theta\partial_y j_x(\boldsymbol{x}_b)+\sin\theta\partial_z j_x(\boldsymbol{x}_b)\right)\\
&-\frac{\delta_r^2}{2}\left(\partial_{yy} j_x(\boldsymbol{x}_b)+\partial_{zz} j_x(\boldsymbol{x}_b)-\frac{1}{r^2}\cancel{\partial_{\theta\theta} j_x(\boldsymbol{x}_b)}\right),
\end{aligned}
\tag{6.19}
$$

where the distance between the wall and the boundary node is:

$$
\delta_r=(\boldsymbol{x}_b-\boldsymbol{x}_w)\cdot\boldsymbol{e}_r \tag{6.20}
$$

with $\boldsymbol{e}_r$ the radial unit vector (aligned with wall normal vector) of the (x,r,θ) system, see Fig. 1.

In Eq. (6.19) the momentum derivatives at $\boldsymbol{x}_b$ follow from solving Eq. (6.4), applied to Eq. (6.16) (regular node) or to Eq. (6.16) augmented by Eq. (6.17) (singular node). The fluid momentum at the wall, $j_x(\boldsymbol{x}_w)$, is determined according to the physical boundary condition, as given in Section 5. For the slip models described in Section 5, the $j_x(\boldsymbol{x}_w)$ may be given by Eq. (5.1) for NL, Eq. (5.2) for NNL, Eq. (5.3) for ASP, or Eq. (5.4) for HZK slip models. Once again, to account for the circular wall geometry, in all these slip models the wall shear stress is mapped onto cylindrical coordinates, $\tau_{ns}\mapsto\tau_{rx}$, so that:

$$
\tau_{rx}(\boldsymbol{x}_w)=\nu(\boldsymbol{x}_w)\partial_r j_x(\boldsymbol{x}_w). \tag{6.21}
$$

As the derivative $\partial_r j_x(\boldsymbol{x}_w)$ is also unknown, this term is once again approximated as a second-order Taylor series, where the relation between wall and boundary node deriva-

tives is expressed as:

$$\begin{aligned}\partial_r j_x(\boldsymbol{x}_w) =& \partial_r j_x(\boldsymbol{x}_b) + \delta_r \partial_{rr} j_x(\boldsymbol{x}_b) \\ =& \left(1-\frac{\delta_r}{r}\right)\left(\cos\theta\partial_y j_x(\boldsymbol{x}_w) + \sin\theta\partial_z j_x(\boldsymbol{x}_w)\right) \\ &+\delta_r\left(\partial_{yy} j_x(\boldsymbol{x}_w) + \partial_{zz} j_x(\boldsymbol{x}_w) - \frac{1}{r^2}\cancel{\partial_{\theta\theta} j_x(\boldsymbol{x}_b)}\right). \end{aligned} \tag{6.22}$$

The viscosity $\nu(\boldsymbol{x}_w)$ in Eq. (6.21) is given by Eq. (4.3), and is again determined with the help of Eq. (6.22) to determine $\partial_r j_x(\boldsymbol{x}_w)$. This exposition concludes the reconstruction of $f_q(\boldsymbol{x}_b)$, as given by Eq. (6.18), which incorporates the slip velocity model, given in Section 5, and the non-Newtonian viscosity law, given in Section 4.

The workflow of the LSOB algorithm, described above, can be summarized as follows:

1. Construct and update the matrix $[\mathbf{M}]$ at each iteration.
2. Select relevant $\hat{n}_q^{\pm}$ populations and assemble vector $\mathcal{N}$ after each collision step.
3. Count $\dim(\mathcal{X})$ and verify whether $\text{rank}[\mathbf{M}] \geq \dim(\mathcal{X})$ or $\text{rank}[\mathbf{M}] < \dim(\mathcal{X})$.
4. If $\text{rank}[\mathbf{M}] \geq \dim(\mathcal{X})$ (regular node) then compute $\mathcal{X} = \{\partial_y j_x(\boldsymbol{x}_b), \partial_z j_x(\boldsymbol{x}_b), \partial_{yy} j_x(\boldsymbol{x}_b), \partial_{zz} j_x(\boldsymbol{x}_b)\}$ from the linear algebra problem $\mathcal{X} = [\mathbf{M}]^{-1}\mathcal{N}$, given by Eq. (6.16).
5. If $\text{rank}[\mathbf{M}] < \dim(\mathcal{X})$ (singular node) then compute $\mathcal{X} = \{\partial_y j_x(\boldsymbol{x}_b), \partial_z j_x(\boldsymbol{x}_b), \partial_{yy} j_x(\boldsymbol{x}_b), \partial_{zz} j_x(\boldsymbol{x}_b), \partial_{yz} j_x(\boldsymbol{x}_b)\}$ from the linear algebra problem $\mathcal{X} = [\mathbf{M}]^{-1}\mathcal{N}$, given by Eq. (6.16) augmented by Eq. (6.17).
6. Determine $\partial_r j_x(\boldsymbol{x}_w)$ based on Eq. (6.22).
7. Determine $\nu(\boldsymbol{x}_w)$ based on Eq. (4.3), using $\partial_r j_x(\boldsymbol{x}_w)$ from Eq. (6.22).
8. Determine $\tau_{xr}(\boldsymbol{x}_w)$ based on Eq. (6.21).
9. Determine $j_x(\boldsymbol{x}_w)$ based on the selected slip boundary model, e.g., Eq. (5.2) for NNL, Eq. (5.3) for ASP, or Eq. (5.4) for HZK slip models, with $\tau_{xy}(\boldsymbol{x}_w)$ given by Eq. (6.9).
10. Compute $j_x(\boldsymbol{x}_b)$ based on Eq. (6.19), using $j_x(\boldsymbol{x}_w)$ and $\mathcal{X} = \{\partial_y j_x(\boldsymbol{x}_b), \partial_z j_x(\boldsymbol{x}_b), \partial_{yy} j_x(\boldsymbol{x}_b), \partial_{zz} j_x(\boldsymbol{x}_b)\}$, to be used in Eq. (6.18).
11. Compute $P(\boldsymbol{x}_b)$ based on Eq. (6.6), to be used in Eq. (6.18).
12. Construct unknown $f_q(\boldsymbol{x}_b)$ populations based on Eq. (6.18) using $j_x(\boldsymbol{x}_b)$ and $P(\boldsymbol{x}_b)$ previously computed in steps 10 and 11.

Remark 6.2. As noted in Remark 6.1 the LSOB algorithm presented here for curved walls also falls into the Lnode formulation. The extension to other LSOB frameworks, such as the Lwall, is straightforward and not pursued here.

7 Numerical tests

To evaluate the accuracy of the LSOB slip boundary schemes, described in Section 6, numerical solutions $j_x^{(\text{num})}$ were compared against analytical one $j_x^{(\text{exact})}$ in two reference canonical problems: (i) 2D slip planar channel flow (in horizontal and diagonal setups), and (ii) 3D circular pipe flow. Both problems are governed by the steady Stokes equation, given by Eq. (2.6). The numerical accuracy is measured as:

$$\|\mathrm{L}_2(j_x)\| = \frac{\sqrt{\sum\left(j_x^{(\text{num})} - j_x^{(\text{exact})}\right)^2}}{\sqrt{\sum\left(j_x^{(\text{exact})}\right)^2}}, \tag{7.1}$$

where sums apply to all non-solid sites within the computational domain.

Numerical tests were implemented as follows. Wall boundary conditions were mostly prescribed with the LSOB approach, although the so-called "kinetic" boundary schemes [25–28, 33] were also tested for the sake of analysis. At the inlet and outlet flow boundaries, periodic boundary conditions were established. The alternative, but equivalent situation of pressure inlet and outlet boundary conditions, with $F_x \to -\partial_x P = (P_{\text{in}} - P_{\text{out}})/\ell$, was also tested (using the Zou and He method [82]). Since the obtained pressure- and force-driven channel flow solutions were confirmed to be equivalent, only the latter will be presented in the manuscript. As for the LBM simulations, all runs were started from an initial equilibrium state, considering a uniform pressure and zero velocity fields. The LBM solution was converged towards steady-state, defined by the criterion: $|\sum j_x(t)/\sum j_x(t-t_a) - 1| < 10^{-12}$, with $t_a = 100$ time steps.

For the problem physical parametrization, we identify the following two Reynolds number definitions: (i) the standard $\mathrm{Re} = \frac{j_{\max} h}{\rho_0 \nu_\infty}$ and (ii) the modified $\mathrm{Re}_{\text{mod}} = \frac{j_{\max}^{2-n} h^n}{a \rho_0}$, see [84, 85]. However, instead of considering them separately, we work with their ratio $\beta = \frac{\mathrm{Re}_{\text{mod}}}{\mathrm{Re}} \in [0,1)$, which permits blending into a single parameter the dynamical behavior ranging between a pure power-law non-Newtonian fluid ($\beta = 0$ and $n \neq 1$) and an asymptotically-pure Newtonian fluid ($\beta \to 1$). As for the slip condition, the non-dimensional group governing the slippage phenomenon can be determined by the dimensionless slip length parameter $\zeta = b/L$ for the case of liquids or the Knudsen number $\mathrm{Kn} = \frac{\lambda}{h}$ for the case of gases. Irrespective of the case, the liquid slip length b or the gas mean free path λ are taken as proportional to the slip measure L_{slip}, in turn defined as $L_{\text{slip}} = \frac{j_{\text{ws}}}{\partial_y j_x(\boldsymbol{x}_w)}$. Fig. 3 illustrates how the imposed slip length must scale with the selected channel resolution

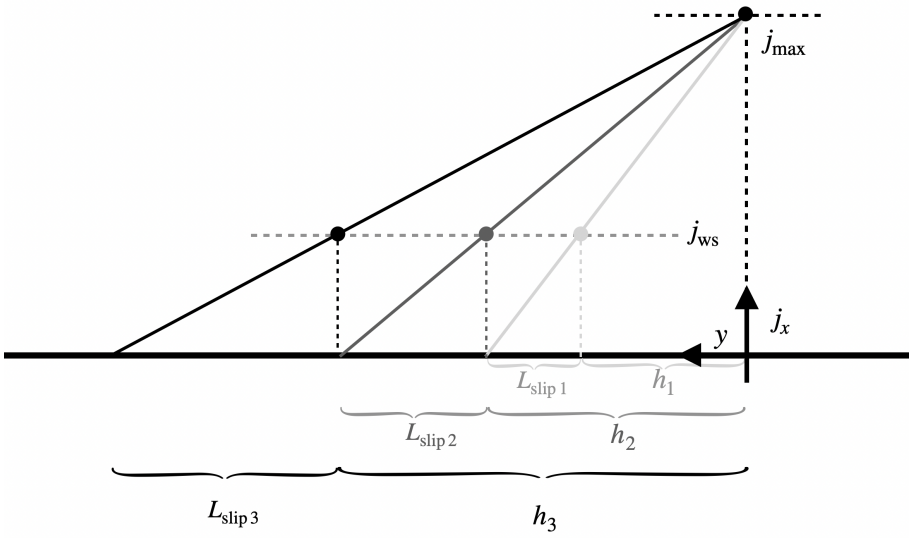

Figure 3: Self similar solutions illustrated across three cases. An increase in the domain resolution (here represented by h) should not result in a change in slip velocity, for a fixed dimensionless slip length (liquids) or the Knudsen number (gases). The slip length (L_{slip}) scales with h to accommodate self-similarity.

in order to guarantee the independence of the slip velocity condition at wall. From self-similarity, one can cast the aforementioned proportionality relation as follows:

$$\frac{j_{ws}}{j_{max}} \propto \frac{L_{slip}}{h+L_{slip}} \propto \begin{cases} \frac{\zeta}{\zeta+1} & \text{for liquids,} \\ \frac{\mathrm{Kn}}{\mathrm{Kn}+1} & \text{for gases.} \end{cases} \tag{7.2}$$

On this basis, the scaling of the imposed external body force term is given as follows:

$$F_x = \frac{1}{\mathrm{Re}_{mod}} \frac{j_{max}^2}{\rho_0 h} \times \begin{cases} \left[\frac{2\beta}{\zeta+1} + \frac{1-\beta}{(\zeta+1)^n}\left(\frac{n+1}{n}\right)^n\right] & \text{for liquids,} \\ \left[\frac{2\beta}{\mathrm{Kn}+1} + \frac{1-\beta}{(\mathrm{Kn}+1)^n}\left(\frac{n+1}{n}\right)^n\right] & \text{for gases.} \end{cases} \tag{7.3}$$

The transcription of the above results to a 3D pipe geometry is direct and only requires replacing the length scale h by $R/2$.

7.1 2D horizontal channel

This section concerns with the application of the LSOB formulas, which were derived in Section 6.1, for a 2D horizontal channel flow subject to linear and non-linear slip laws at walls and obeying Newtonian or non-Newtonian fluid rheology. First, Subsection 7.1.1 presents the analytical solutions of the problem used to benchmark the developed numerical schemes. Then, the accuracy performance of those schemes is discussed in Subsection 7.1.2.

7.1.1 Analytical solutions

Consider a flow moving between two infinite parallel plane walls as sketched in Fig. 1(a). The top and bottom walls are stationary, and feature the same slip coefficients and choice of slip models. This makes the velocity profile symmetric about the channel centerline $\partial_y j_x(0)=0$. For a Newtonian fluid, the analytical solution of the velocity profile is

$$j_x(y)=-\frac{F_x}{2\nu}\left(y^2-h^2\right)+j_x(h), \tag{7.4}$$

where the content of $j_x(h)$ is dictated by the slip law and its explicit value is summarized in Table 1.

When the fluid is non-Newtonian, the derivation of analytical solutions becomes a much more challenging task. Skipping details and referring to the work [16] for more information, the analytical solutions of a Sisko law fluid for $\beta\in[0,1)$ are given bellow for two particular exponents; namely, for the non-Newtonian exponent $n=1/2$:

$$j_x(y)=-\frac{F_x\left(y^2-h^2\right)}{2\nu_\infty}+\frac{a^2(-|y|+h)}{2\nu_\infty^2}-\frac{a\left(\left(a^2+4\nu_\infty F_x h\right)^{\frac{3}{2}}-\left(a^2+4\nu_\infty F_x|y|\right)^{\frac{3}{2}}\right)}{12\nu_\infty^3 F_x}+j_x(h) \tag{7.5}$$

and for the non-Newtonian exponent $n=2$:

$$j_x(y)=\frac{\nu_\infty}{2a}(|y|-h)-\frac{\left(\nu_\infty^2+4aF_x|y|\right)^{\frac{3}{2}}-\left(\nu_\infty^2+4aF_x h\right)^{\frac{3}{2}}}{12a^2F_x}+j_x(h). \tag{7.6}$$

For the particular case of a power-law viscosity fluid ($\beta=0$), general solutions $\forall\, n\in\mathbb{R}^+$ are given as follows [16]:

$$j_x(y)=\left(\frac{F_x}{a}\right)^{\frac{1}{n}}\frac{n}{n+1}(h^{1+\frac{1}{n}}-|y|^{1+\frac{1}{n}})+j_x(h). \tag{7.7}$$

The content of $j_x(h)$ in Eq. (7.7) is established by the chosen slip law and is again given in Table 1.

Table 1: Slip momentum for the different slip laws given in Section 5, considering a resting wall $j_{\text{wall}}=0$ and $F_x>0$, with $j_x(h)$ the momentum value at the wall taken as $j_x(h)=j_{\text{ws}}=\frac{\zeta}{\zeta+1}j_{\max}$ (liquids) or $j_x(h)=j_{\text{ws}}=\frac{\text{Kn}}{\text{Kn}+1}j_{\max}$ (gases).

	Navier	**Non-linear Navier**	**Asymptotic**	**Hatzikiriakos**
$j_x(h)$	$k_l F_x h$	$k_{nl}\lvert F_x h\rvert^{m-1}F_x h$	$k_{a1}\ln(1+k_{a2}F_x h)$	$k_{h1}\sinh(k_{h2}F_x h-\tau_c)$

7.1.2 Numerical solutions

In LBM, the 2D geometry is discretized on the D2Q9 lattice, featuring the following spatial domain parameters: $N_x = 3$ computational cells along the channel flow horizontal direction and a varying number of N_y computational cells along the wall normal vertical direction, which will be specified ahead.

First, the LBM simulation of a Newtonian fluid is studied. Here, focus is put on the accuracy of the LSOB boundary scheme described in Section 6.1 to prescribe the no-slip, linear slip and non-linear slip boundary laws. In all cases it is confirmed that LBM numerical solutions reproduce exactly (up to the machine accuracy) the analytical velocity profiles, regardless the wall boundary node distance $\delta_y \in [0,1]$, the values of the mesh resolution N_y or the TRT relaxation parameter Λ. Note that, as the analytical profiles remain given by a parabola with a constant shift at walls, even with non-linear slip laws, the results of this test provide a numerical proof of the parabolic accuracy of the LSOB scheme on plane walls.

Next, the study is repeated for a non-Newtonian fluid, considering as boundary conditions the no-slip, Navier linear slip and Navier non-linear slip laws. Fig. 4 shows the obtained mesh convergence results; as illustrative values we take $\Lambda = 3/16$ and the wall boundary node distance of $\delta_y = 1/4$ (other δ_y distances will be discussed ahead). Numerical results indicate that the LSOB scheme is able to accommodate the different physical wall boundary conditions, no-slip or slip (with either linear or non-linear laws), under roughly identical accuracies. Since the asymptotic and Hatzikiriakos non-linear slip laws produce very similar results compared to the Navier non-linear slip solutions, our presentation is limited to the Navier non-linear slip model, setting the exponent $m = 2$ for concreteness. As for the non-Newtonian model, the power-law exponent n noticeably affects the error magnitude. Yet, the error still decreases with second-order rate in mesh resolution. The fact that the magnitude of the numerical error is essentially controlled by the non-Newtonian model and not by the boundary law is a sign that, with the LSOB scheme, the main error source is coming from bulk, i.e. it comes from the approximation of the non-Newtonian profile. On the contrary, the reproduction of the very same numerical tests, but employing the so-called "kinetic" LBM boundary schemes [25–28, 33], indicates that the main error source is determined by the boundary model. In this case, the numerical accuracy of the LBM solution becomes severely degraded, reducing its convergence rate to first-order in the no-slip case and further diminishing to the zeroth-order (i.e. lack of convergence) in the slip regime (with either linear or non-linear laws). Although not shown here, these outcomes follow the trends showed in previous published works [33, 34, 37] concerning the lack of convergence of LBM with "kinetic" boundary schemes when modeling channel flows subject to the standard Navier linear slip velocity boundary condition.

Figs. 5 and 6 display the effect of the TRT relaxation parameter Λ on the numerical error, respectively, considering a coarse mesh $N_y = 12$ and a fine mesh $N_y = 96$ resolution, respectively. As previously denoted, for a Newtonian fluid, $n = 1$, the $j_x(y)$ solution

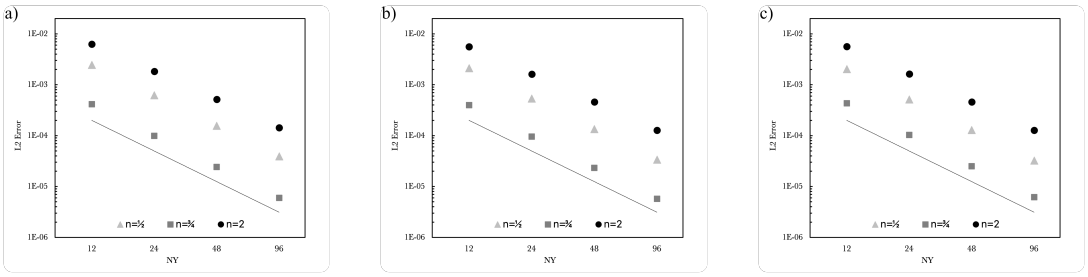

Figure 4: Mesh convergence plots in a 2D channel using the LSOB scheme, with $\delta_y=1/4$ wall boundary node distance, fixing $\Lambda=3/16$, for a non-Newtonian power-law fluid with exponents $n=1/2$ (triangle), $n=3/4$ (square) and $n=2$ (circle), where continuous straight line indicates a slope -2. Panel (a): No-slip BC ($\zeta=0$ or $\mathrm{Kn}=0$). Panel (b): Navier linear slip BC ($\zeta=0.1$ or $\mathrm{Kn}=0.1$). Panel (c): Navier non-linear slip BC ($\zeta=0.1$ or $\mathrm{Kn}=0.1$ and $m=2$).

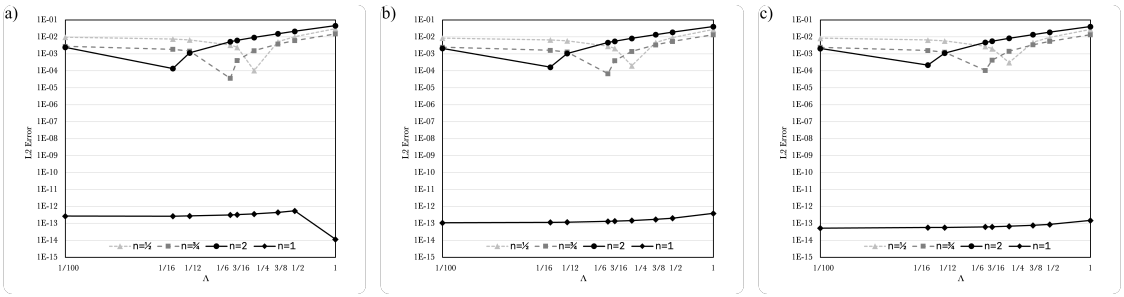

Figure 5: Effect of TRT relaxation parameter Λ in a 2D channel on the numerical error with LSOB scheme, on a coarse mesh ($N_y=12$), for a Newtonian fluid $n=1$ (diamond) and non-Newtonian power-law fluid with exponents $n=1/2$ (triangle), $n=3/4$ (square) and $n=2$ (circle). Panel (a): No-slip BC ($\zeta=0$ or $\mathrm{Kn}=0$). Panel (b): Navier linear slip BC ($\zeta=0.1$ or $\mathrm{Kn}=0.1$). Panel (c): Navier non-linear slip BC ($\zeta=0.1$ or $\mathrm{Kn}=0.1$ and $m=2$). All cases consider the arbitrary $\delta_y=1/4$ wall boundary node distance.

is parabolic. Therefore, the LSOB scheme is able to accommodate this parabolic profile exactly on boundaries, regardless a no-slip or a slip model is being considered. In other words, for $n=1$, the LBM solution with the LSOB scheme agrees exactly with the analytical velocity profile $\forall\,\Lambda$. Note that the slight increase of the numerical error at $\Lambda=1/100$ for the fine mesh case, Fig. 6, is due to the accumulation of round-off errors. For a non-Newtonian fluid, $n\neq1$, the flow profile is no longer parabolic. Therefore, deviations from the analytical solution become unavoidable. Numerical experiments on the error in this case indicate that the accuracy reaches a minimum at a particular Λ value, which we will designate as Λ_{opt}. This Λ_{opt} value tends to hold with the mesh refinement, although the overall magnitude of the error observed at Λ_{opt} decreases in accordance to the scheme numerical convergence. Fixing the power-law exponent n, the value of Λ_{opt} is also found to be roughly insensitive to the wall law or the mesh resolution. However, when varying the power-law exponent n the Λ_{opt} value gets strongly affected. This again confirms that, with the usage of the LSOB scheme, the dominant error comes from the bulk approximation, whose solution is determined by n.

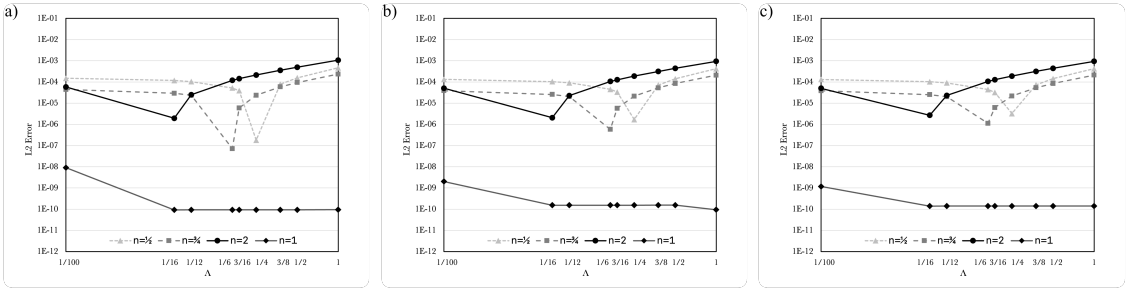

Figure 6: Similar to Fig. 5, but on a fine mesh ($N_y=96$).

Table 2: Order of convergence of the L2 Error given by the slope of the least-squared line computed over $N_y=\{12,24,32,48,96\}$ for the Navier non-linear law with $\zeta=0.1$ or $\mathrm{Kn}=0.1$ and $m=2$ (but shared by all slip models). Label "Exact" indicates that numerical and analytical solutions match (up to the machine precision accuracy) for the $\{\Lambda,n\}$-pair and $\delta_y=0$, independently of mesh resolution.

	$\delta_y=0$			$\delta_y=1/4$			$\delta_y=1/2$			$\delta_y=3/4$		
Λ	$n=1/2$	$n=3/4$	$n=2$	$n=1/2$	$n=3/4$	$n=2$	$n=1/2$	$n=3/4$	$n=2$	$n=1/2$	$n=3/4$	$n=2$
$1/100$	-2.07	-2.05	-1.84	-2.00	-1.99	1.79	1.91	-1.93	-1.73	-1.77	-1.83	-1.66
$1/16$	-2.07	-2.05	-2.07	-2.00	-1.99	-2.12	1.90	-1.91	-2.12	-1.75	-1.81	-2.08
$1/12$	-2.07	-2.05	-1.88	-2.00	-1.99	-1.85	-1.90	-1.90	-1.87	-1.74	-1.81	-1.92
$1/6$	-2.07	-2.92	-1.86	-1.99	-2.19	-1.82	-1.85	-2.19	-1.80	-1.94	-2.18	-1.79
$3/16$	-2.07	-2.08	-1.85	-1.99	-2.04	-1.82	-1.83	-2.07	-1.80	-2.18	-2.14	-1.78
$1/4$	Exact	-2.06	-1.85	-2.19	-2.01	-1.82	-2.29	-1.99	-1.79	-2.27	-2.01	-1.77
$1/2$	-2.07	-2.05	-1.85	-2.01	-2.00	-1.82	-1.97	-1.96	-1.78	-1.97	-1.93	-1.76
1	-2.07	-2.05	-1.85	-2.01	-2.00	-1.81	-1.95	-1.95	-1.78	-1.92	-1.92	-1.75

Table 2 lists the order of mesh convergence for the Navier non-linear law, modelled with the LSOB model, as function of (i) the TRT relaxation parameter Λ, (ii) the power-law exponent n, and (iii) the wall-boundary node distance δ_y. From this table the following conclusions can be drawn. First, despite second-order convergence being fairly persistent throughout all n power-law exponents, the order of convergence has a slight tendency to decrease as n increases. Second, for lower values of δ_y, namely $\delta_y\leq 1/2$, the choice of $\Lambda\neq\Lambda_{\mathrm{opt}}$ shows little effect on the global convergence value. Third, gains in convergence are marginal when Λ approaches Λ_{opt}, suggesting the rather localized effect of Λ_{opt}.

Table 2 also indicates that, when $\delta_y=0$, the LBM-TRT with the LSOB scheme manages to exactly reproduce the analytical solution for very specific $\{n,\Lambda_{\mathrm{opt}}\}$ combinations. Namely, the pair $\{n=1/2,\Lambda_{\mathrm{opt}}=1/4\}$ (and also $\{n=1/3,\Lambda_{\mathrm{opt}}=3/8\}$, although not shown here) makes the LBM solutions machine-accurate with respect to the analytical ones, which are given by cubic polynomials when $n=1/2$ (or quartic polynomials when $n=1/3$). Inspired by these findings, we proceed to assess in more detail the interplay between Λ_{opt} and the power-law exponent n. The results of this study are collected in Table 3. This table reveals that Λ_{opt} decreases with the power-law exponent n increase,

Table 3: Pairs $\{n,\Lambda_{\text{opt}}\}$ that minimize the L2 Error for the Navier non-linear law with $\zeta=0.1$ or $\text{Kn}=0.1$ and $m=2$ (but shared by all slip models), and using the LSOB model $\delta_y\in[0,1]$.

n	Λ_{opt}
1/2	1/4
2/3	3/16
3/4	1/6
3/2	1/12

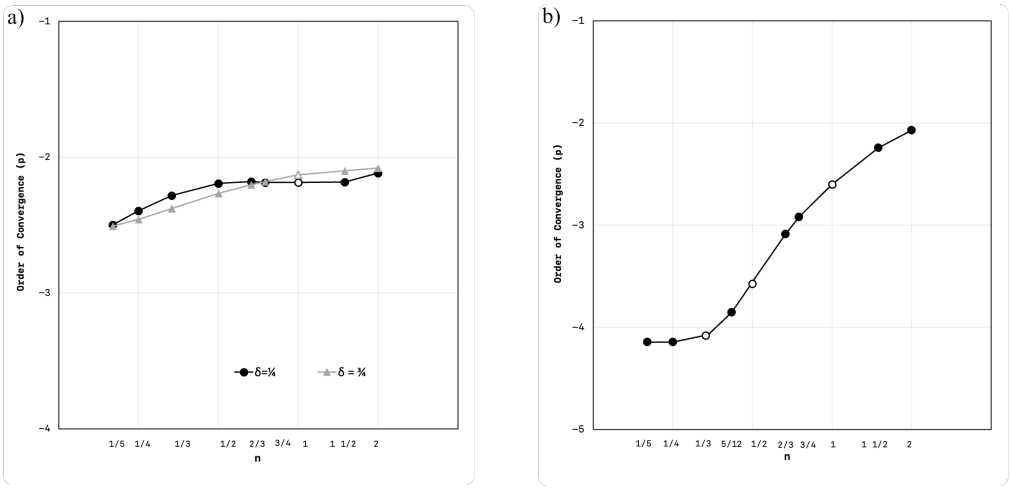

Figure 7: Order of convergence of L2 Error computed over $N_y=\{12,24,32,48,96\}$ for the Navier non-linear law with $\zeta=0.1$ or $\text{Kn}=0.1$ and $m=2$ (but shared by all slip models), and using $\Lambda=\Lambda_{\text{opt}}$, as function of the power-law exponent n using the LSOB scheme. Panel (a): Setting $\delta_y=1/4$ and $\delta_y=3/4$. Panel (b): Setting $\delta_y=0$. In panel (b), the hollow markers in both panels denote singularities in the continuous line; they correspond to the cases $n=1/2$ and $n=1/3$ where the rate of convergence is not defined since numerical and analytical solutions exactly match at $\Lambda=\Lambda_{\text{opt}}$.

permitting to establish the following relationship $\Lambda_{\text{opt}}=\frac{1}{8n}$. Note that, with the exception of the aforementioned two pairs (and obviously the Newtonian case $\{n=1,\forall\Lambda\}$), the majority of $\{n,\Lambda_{\text{opt}}\}$ combinations does not lead to exact LBM solutions. Fig. 7 plots the evolution of the order of convergence of the L2 Error as function of the power-law exponent n, with Λ_{opt} chosen accordingly. For $\delta_y\neq 0$, the calibration of Λ may push the order of convergence below -2, but it does not completely eliminate the $\mathcal{O}(\delta_y^2)$ error terms. Consequently, the scheme does never effectively become higher-order accurate, see Fig. 7(a). For $\delta_y=0$, the LSOB scheme is not limited by the intrinsic $\mathcal{O}(\delta_y^2)$ accuracy of the second-order Taylor expansion to approximate the physical boundary condition. Therefore, in this case, the LBM solution may support higher-order accuracy, providing the bulk error can be cancelled by a proper Λ calibration. Fig. 7(b) illustrates this study

and it shows that the possibility of improving the scheme convergence rate through Λ_{opt} is particularly noticeable when modeling shear thinning fluids, $n<1$, where global third-order accuracy is met at $1/3<n<2/3$ while fourth-order accuracy is reached for $n\leq 1/3$, see Fig. 7(b). These results shed light on the structure of the LBM numerical errors and provide guidelines for future theoretical analyses on the LBM modeling of power-law non-Newtonian fluids.

7.2 2D diagonal inclined channel

This section extends the horizontal channel flow simulations, presented in Section 7.1, to an inclined setup, considering the case where the channel aligns with the lattice diagonal links. The analytical solutions presented in Section 7.1.1 hold, but are subject to the reference frame transformation $(x,y)\mapsto(x',y')$, featuring $\theta=\pi/4$. The diagonal channel is discretized on the D2Q9 uniform mesh. A sketch of the discretization is illustrated in Fig. 2. The LSOB formulation presented in Section 6.2 is used to prescribe the wall boundary condition. As theoretically demonstrated, this LSOB scheme is able to prescribe the intended slip law at the desired location, within a parabolic level of accuracy. The goal of this section is to demonstrate, based on numerical tests, that the designed parabolic accuracy is also verified when the walls are rotated on the mesh.

7.2.1 Analytical solutions

The analytical solutions for the 2D inclined channel flow problem considered here can be obtained from those presented in Subsection 7.1.1, by considering the mapping $(x,y)\mapsto(x',y')$ with $\theta=\pi/4$. For example, the analytical solution of a velocity profile for a non-Newtonian (power-law) fluid, which for a 2D horizontal channel is given by Eq. (7.7), now reads:

$$j_{x'}(y')=\left(\frac{F_{x'}}{a}\right)^{\frac{1}{n}}\frac{n}{n+1}\left(h'^{1+\frac{1}{n}}-|y'|^{1+\frac{1}{n}}\right)+j_{x'}(h'), \tag{7.8}$$

where $h'=h\cos\theta$ and the mapping of vectorial quantities to the (x',y') frame is given as $y'=-x\sin\theta+y\cos\theta$, $j_{x'}=-j_x\sin\theta+j_y\cos\theta$, etc. By following these transformation rules, all other solutions presented in Subsection 7.1.1 can be easily transposed to the inclined channel geometry. Likewise, the content of $j_{x'}(h')$ in Eq. (7.8) is dictated by the wall slip law, given by Table 1, but subject to the frame transformations above indicated.

7.2.2 Numerical solutions

In LBM, the 2D geometry is discretized on the D2Q9 lattice, considering a spatial domain with $N_x=N_y$ computational cells (their values will be specified ahead). The numerical tests presented in Subsection 7.1.2 are now repeated for the 2D diagonal inclined channel.

First, the simulation of a Newtonian fluid is considered. The analytical solution of this case is given by Eq. (7.8) with the power-law exponent $n=1$. The focus of the analysis is

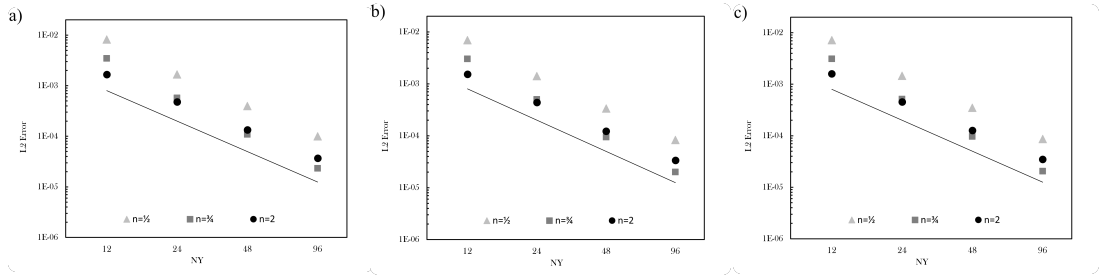

Figure 8: Mesh convergence plots in a 2D diagonal inclined channel using the LSOB scheme, with $\delta_{y'}=\delta_y\cos\theta=\frac{1}{4}\frac{\sqrt{2}}{2}$ wall boundary node distance, fixing $\Lambda=3/16$, for a non-Newtonian power-law fluid with exponents $n=1/2$ (triangle), $n=3/4$ (square) and $n=2$ (circle), where continuous straight line indicates a slope -2. Panel (a): No-slip BC ($\zeta=0$ or $\mathrm{Kn}=0$). Panel (b): Navier linear slip BC ($\zeta=0.1$ or $\mathrm{Kn}=0.1$). Panel (c): Navier non-linear slip BC ($\zeta=0.1$ or $\mathrm{Kn}=0.1$ and $m=2$).

on the accuracy of the LSOB scheme described in Section 6.2 and how they prescribe the no-slip, linear slip or non-linear slip boundary laws over inclined flat walls. It is numerically confirmed that the proposed LSOB scheme leads to LBM numerical solutions that exactly reproduce (up to the machine accuracy) the analytical velocity profiles, regardless of the wall boundary node distance $\delta_{y'}$, the values of the mesh resolution N_y or the TRT relaxation parameter Λ, in all cases of boundary conditions studied herein.

Next, the study is extended for a non-Newtonian fluid, once again considering the no-slip, linear slip or non-linear slip laws as boundary conditions for the diagonal inclined channel. Fig. 8 shows the obtained mesh convergence results, obtained for the arbitrary values $\Lambda=3/16$ and $\delta_{y'}=\delta_y\cos\theta=\frac{1}{4}\frac{\sqrt{2}}{2}$. Numerical simulations reveal that the LSOB scheme is able to accommodate the different physical wall boundary conditions, no-slip or slip (with either linear or non-linear laws), under roughly identical accuracies following a second-order rate of convergence. Note that since asymptotic and Hatzikiriakos non-linear slip laws produce very similar results compared to the Navier non-linear slip solutions, the results here presented are limited to the Navier non-linear slip model, setting the exponent $m=2$ for concreteness. Contrary to the wall slip law model, the non-Newtonian power-law exponent n seems to play a more meaningful role on the accuracy of solutions. These trends are in line with the horizontal channel simulations presented in Subsection 7.1.2.

Figs. 9 and 10 display the effect of the TRT relaxation parameter Λ on the numerical accuracy, considering coarse $N_y=12$ and fine $N_y=96$ meshes, respectively. As expected, the Newtonian fluid $n=1$ is exactly reproduced by the LBM solution, which provides a numerical demonstration for the parabolic accuracy of the LSOB scheme, also on inclined straight walls. In the non-Newtonian $n\neq1$ case, the LSOB solutions are barely unaffected by Λ on both mesh refinement scenarios. The exploration of an optimal Λ value, which guarantees the lower error, is not so evident in this case as compared to the horizontal channel setup. Nonetheless, it is confirmed that, with the LSOB scheme modeling the boundary condition, the dominant error source comes from the bulk approximation of

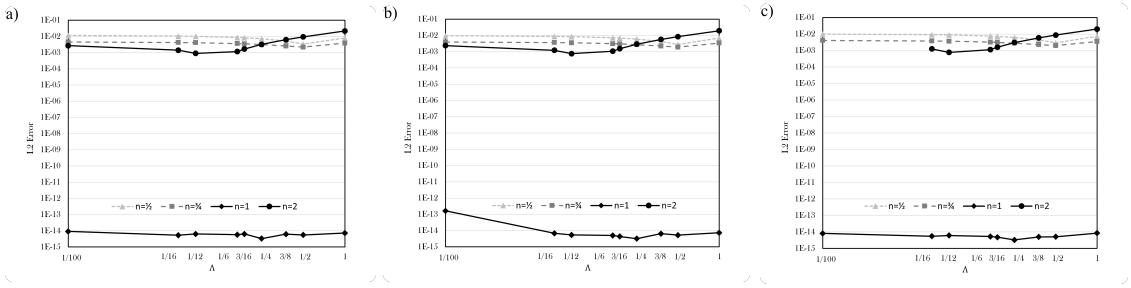

Figure 9: Effect of TRT relaxation parameter Λ in a 2D diagonal inclined channel on the numerical error with LSOB scheme, on a coarse mesh (N_y=12), for a Newtonian fluid n=1 (diamond) and non-Newtonian power-law fluid with exponents $n=1/2$ (triangle), $n=3/4$ (square) and $n=2$ (circle). Panel (a): No-slip BC ($\zeta=0$ or $\mathrm{Kn}=0$). Panel (b): Navier linear slip BC ($\zeta=0.1$ or $\mathrm{Kn}=0.1$). Panel (c): Navier non-linear slip BC ($\zeta=0.1$ or $\mathrm{Kn}=0.1$ and $m=2$). All cases consider the generic value $\delta_{y'}=\delta_y\cos\theta=\frac{1}{4}\frac{\sqrt{2}}{2}$ for the wall boundary node distance.

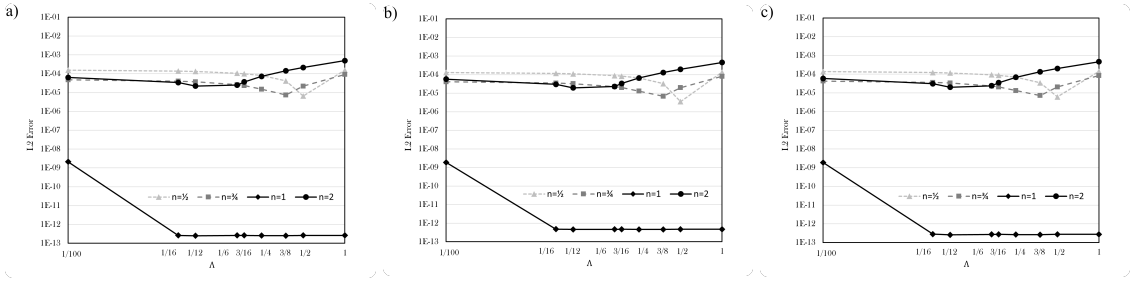

Figure 10: Similar to Fig. 5, but on a fine mesh (N_y=96).

the non-Newtonian velocity profiles. This observation attests the high level of accuracy of the proposed LSOB schemes so that its usage typically guarantees the boundary error to be smaller than the bulk error.

7.3 3D circular tube

This section concerns with the application of the LSOB formulae, which were derived in Section 6.3, for a flow inside a 3D circular tube with walls subject to linear and non-linear slip laws, where the fluid may display Newtonian or non-Newtonian behavior. Subsection 7.3.1 presents the analytical solutions of this problem. Then, Subsection 7.3.2 discusses the accuracy of the developed numerical schemes in this setup. Compared to the 2D test case addressed in Section 7.1, the new specific challenge here lies in the modeling of the slip velocity boundary condition on a 3D geometry with curved shaped walls.

7.3.1 Analytical solutions

Consider the flow through a circular tube of constant cross-section as sketched in Fig. 1(b). Solutions to this problem can be obtained from the 2D channel case, previously presented in Subsection 7.3.1, by employing the substitutions $y \to r$ and $h \to R$. For example, the analytical solution of the velocity profile for a non-Newtonian (power-law) fluid, which for a 2D horizontal channel is given by Eq. (7.7), now reads:

$$j_x(r) = \left(\frac{F_x}{2a}\right)^{\frac{1}{n}} \frac{n}{n+1}\left(R^{1+\frac{1}{n}} - r^{1+\frac{1}{n}}\right) + j_x(R). \tag{7.9}$$

Similarly to Eq. (7.7), the content of $j_x(R)$ is dictated by the wall slip law, given by Table 1 with the substitution $h \to R/2$. All other solutions presented in Subsection 7.1.1, including the slip laws $j_x(R)$ given by Table 1, are easily transposed to the 3D pipe geometry by performing the same transformations.

7.3.2 Numerical solutions

In LBM, the 3D geometry is discretized on the D3Q19 lattice, with the following spatial domain discretization parameters considered: $N_x = 3$ computational cells along the channel flow direction and a varying number of $N_y = N_z = R$ computational cells in the cross-sectional plane, which will be specified ahead.

The LBM simulation of a Newtonian fluid inside a 3D pipe, like in the 2D channel case, yields solutions that exactly coincide (up to the machine accuracy) with the analytical parabolic solutions when the LSOB scheme is used for no-slip, linear slip or non-linear slip velocity boundary conditions, regardless of the value of numerical parameters employed, such as the mesh resolution N_y or the TRT relaxation function Λ. In contrast, the use of the "kinetic" boundary schemes [25–28,33] to model this 3D geometry deteriorates the accuracy of LBM solutions to first-order in the no-slip case or zeroth-order in the slip case; while not shown in the manuscript this result agrees with previously published studies [37].

Fig. 11 shows the mesh convergence behavior, in the range $N_y = N_z = R \in [12, 96]$, obtained for a non-Newtonian fluid inside the 3D pipe subject to several boundary conditions, such as the no-slip, Navier linear slip and Navier non-linear slip laws (with $m = 2$), modeled with the LSOB scheme, fixing $\Lambda = 3/16$ as illustrative value; asymptotic and Hatzikiriakos non-linear slip laws are not shown as they produce similar solutions to Navier non-linear slip law. This test shows a quantitative dependence between the type of non-Newtonian model, as determined by the exponent n, and the type of wall condition, on the accuracy of the LBM solution. For small n the solution accuracy is roughly insensitive to the type of wall condition, whereas the accuracy of large n solutions tends to deteriorate when shifting the wall condition from no-slip to the non-linear slip case. Still, close to second-order mesh convergence is maintained for all cases.

Figs. 12 and 13 display the effect of the TRT relaxation parameter Λ on the numerical error, respectively, considering a coarse mesh $R = 12$ and a fine mesh $R = 96$ resolution.

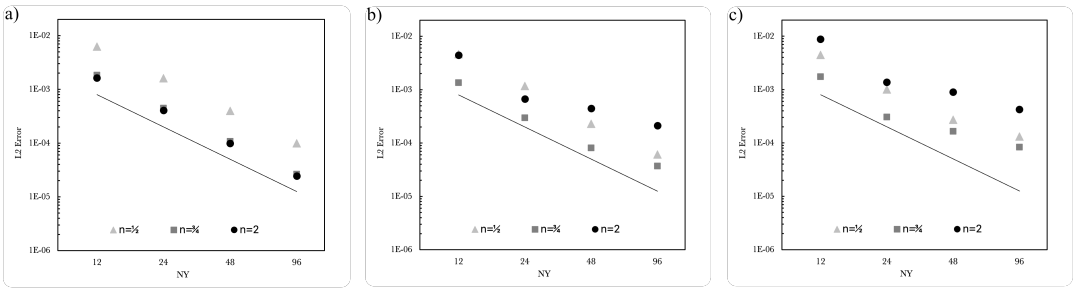

Figure 11: Mesh convergence plots in a 3D pipe using the LSOB scheme, fixing $\Lambda=3/16$, for a non-Newtonian power-law fluid with exponents $n=1/2$ (triangle), $n=3/4$ (square) and $n=2$ (circle), where continuous straight line indicates a slope -2. Panel (a): No-slip BC ($\zeta=0$ or $\mathrm{Kn}=0$). Panel (b): Navier linear slip BC ($\zeta=0.1$ or $\mathrm{Kn}=0.1$). Panel (c): Navier non-linear slip BC ($\zeta=0.1$ or $\mathrm{Kn}=0.1$ and $m=2$).

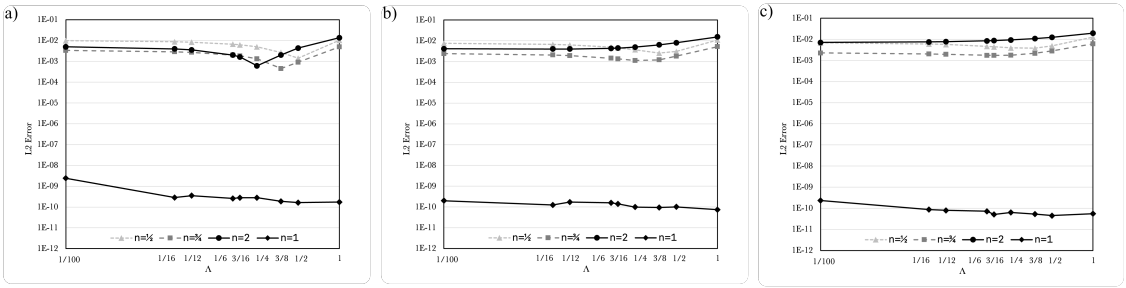

Figure 12: Effect of TRT relaxation parameter Λ in a 3D pipe on the numerical error with LSOB scheme, on a coarse mesh ($R=N_y=N_z=12$), for a Newtonian fluid $n=1$ (diamond) and non-Newtonian power-law fluid with exponents $n=1/2$ (triangle), $n=3/4$ (square) and $n=2$ (circle). Panel (a): No-slip BC ($\zeta=0$ or $\mathrm{Kn}=0$). Panel (b): Navier linear slip BC ($\zeta=0.1$ or $\mathrm{Kn}=0.1$). Panel (c): Navier non-linear slip BC ($\zeta=0.1$ or $\mathrm{Kn}=0.1$ and $m=2$).

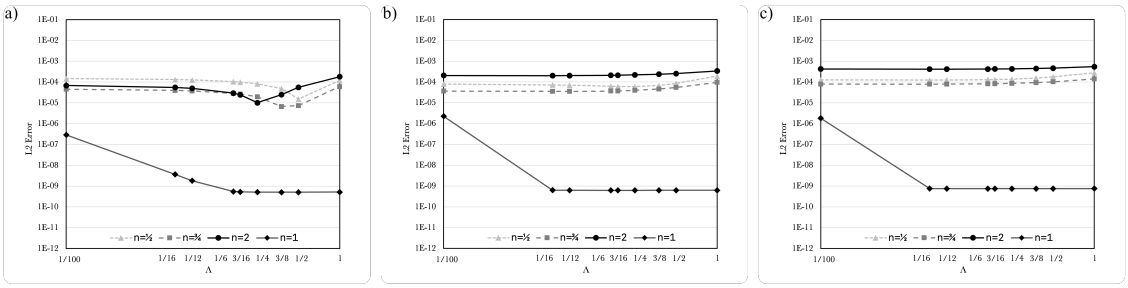

Figure 13: Similar to Fig. 12, but on a fine mesh ($R=N_y=N_z=96$).

Once again, for a Newtonian fluid, $n=1$, the $j_x(y)$ parabolic solution is exactly recovered by LBM with the LSOB scheme, regardless of considering a no-slip or a slip model. This attests the parabolic accuracy of the developed LSOB scheme. For a non-Newtonian fluid, $n\neq 1$, the flow profile is no longer exactly captured. Regardless of the mesh resolution, the effect of Λ on the numerical solution accuracy is now markedly affected by

the wall law. The LSOB modeling of the no-slip condition shows an order of magnitude reduction in error between $\Lambda = 3/16$ and $\Lambda = 1/4$, whereas the LSOB modeling of the slip condition (either linear or non-linear) becomes almost Λ independent. Comparisons between coarse and fine grid cases suggest that the main error source is principally due to the spatial discretization of the boundary condition. Moreover, the fact that the qualitative behavior of the L2 Error vs Λ curves is roughly insensitive to the fluid rheology, as given by the n exponent value (providing $n \neq 1$), also suggests the main error source coming from the boundary discretization, rather than the bulk. Hence, contrary to the lattice aligned 2D planar flow simulation, in this 3D curved boundary geometry there is very little room to improvement through the Λ tuning. Nonetheless, even without the help of the TRT relaxation parameter, the developed boundary scheme is still able to reach a parabolic level of accuracy at all cases.

8 Conclusions

This work was developed with the purpose of advancing the LBM modeling of the steady state and slow viscous flow of both Newtonian and non-Newtonian fluids (described by Sisko model) inside microchannels of planar and circular cross-section when subject to different kinds of wall boundary conditions, potentially described by no-slip, linear slip and non-linear slip laws.

As an accurate and robust strategy to model this problem class, we proposed the use of the two-relaxation-time (TRT) collision model together with the local second order boundary (LSOB) scheme. In this regard, the LSOB scheme had to be reformulated to deal with the specificities of the physical model at hands, namely: (i) the parameters of the non-Newtonian rheological model had to be incorporated into the reconstruction of the LSOB boundary populations, and (ii) to incorporate the non-linear wall slip laws (given by non-linear Navier, empirical asymptotic and Hatzikiriakos laws), the normal Taylor-type condition used to approximate the physical boundary condition onto the LSOB boundary condition had to be subject to specific changes. The application of the proposed LBM boundary scheme was here developed in a step-by-step fashion for both planar and curved walls taking into account 2D and 3D domains, respectively. The generalization to other geometrical cases is easily extendable by following the theory presented in the manuscript. In terms of numerical characteristics, the developed LSOB schemes offer numerous advantages. Among the most important, they preserve the viscosity-independent property of the TRT model with respect to the numerical errors and are able to prescribe the non-linear wall slip laws with parabolic accuracy, which can be considered as state-of-the-art level of accuracy within the second-order accuracy of the standard LBM. Numerical tests, presented at the end of the work, confirmed the superior characteristics of the developed LSOB schemes when applied to the modeling of complex fluid flows inside microchannels.

The extension of the present work to other problem classes is planned for future stud-

ies. To this end, the next logical step will be equipping the current LSOB scheme with the ability to support (i) time-dependent effects and (ii) non-linear fluid convection phenomena. As for the first issue, this task will require the consideration of the time variable in the Taylor series approximation of the boundary node fluid momentum towards the fluid momentum at the wall together with the inclusion of the unsteady contributions into the reconstruction of the boundary populations $f_q(\boldsymbol{x}_b,t)$. As for the second point, the reconstruction of $f_q(\boldsymbol{x}_b,t)$ will also need to incorporate the momentum non-linear terms. We note that the inclusion of both these contributions in the LSOB formulation has been attempted in previous works [86–88], but they relied on a less precise linear approximation. The upgrading of these ideas to parabolic accuracy could explore the developments recently reported in the work [89] (in particular the guidelines given in Section III.A of [89]). It is also worth pointing out that the applicability of the LSOB technique is not limited to Navier-Stokes based problems, but it has also been used in the modeling of Dirichlet and Neumann normal boundary conditions for advection-diffusion equations [90]. Finally, as a last important step in this research topic, it is also proposed the reformulation of the present LSOB algorithm in order to extend it from the Cartesian or cylindrical coordinate frameworks considered here towards a generalized curvilinear coordinate system capable of describing boundaries of arbitrary shape in line with the body-fitted CFD philosophy but focused on the boundary contour [88].

Acknowledgments

The authors acknowledge Fundação para a Ciência e a Tecnologia (FCT) for its financial support via the project LAETA Base Funding (DOI: 10.54499/UIDB/50022/2020). Goncalo Silva is also thankful to Irina Ginzburg for the enlightening discussions on the LSOB method.

Appendices

A Mathematical background: Change of coordinates

A.1 Rotated Cartesian coordinate system

For the sake of completeness, this section summarizes the mathematical apparatus underpinning the mapping between *fixed and rotated Cartesian* systems $(x,y)\mapsto(x',y')$ given by:

$$\begin{cases} x = x'\cos\theta - y'\sin\theta, \\ y = x'\sin\theta + y'\cos\theta, \end{cases} \qquad \begin{cases} j_x = j_{x'}\cos\theta - j_{y'}\sin\theta, \\ j_y = j_{x'}\sin\theta + j_{y'}\cos\theta. \end{cases} \tag{A.1}$$

This mapping $(x,y)\mapsto(x',y')$ applied to first-order momentum derivatives reads:

$$\begin{cases} \partial_x j_x = \cos^2\theta\partial_{x'}j_{x'} - \cos\theta\sin\theta\left(\partial_{x'}j_{y'}+\partial_{y'}j_{x'}\right)+\sin^2\theta\partial_{y'}j_{y'}, \\ \partial_y j_x = \cos\theta\sin\theta\left(\partial_{x'}j_{x'}-\partial_{y'}j_{y'}\right)+\cos^2\theta\partial_{y'}j_{x'}-\sin^2\theta\partial_{x'}j_{y'}, \\ \partial_x j_y = \cos\theta\sin\theta\left(\partial_{x'}j_{x'}-\partial_{y'}j_{y'}\right)-\sin^2\theta\partial_{y'}j_{x'}+\cos^2\theta\partial_{x'}j_{y'}, \\ \partial_y j_y = \sin^2\theta\partial_{x'}j_{x'}+\cos\theta\sin\theta\left(\partial_{x'}j_{y'}+\partial_{y'}j_{x'}\right)+\cos^2\theta\partial_{y'}j_{y'}, \end{cases} \tag{A.2}$$

and to second-order momentum derivatives is given by:

$$\begin{cases} \partial_{xy} j_x = \cos\theta(\cos^2\theta-2\sin^2\theta)\partial_{x'y'}j_{x'} - \sin\theta\cos^2\theta\partial_{y'y'}j_{x'} \\ \qquad -\sin^2\theta\cos\theta\partial_{x'x'}j_{y'}+\sin\theta(\sin^2\theta-2\cos^2\theta)\partial_{x'y'}j_{y'}, \\ \partial_{yy} j_x = 3\cos^2\theta\sin\theta\partial_{x'y'}j_{x'}+\cos^3\theta\partial_{y'y'}j_{x'} \\ \qquad -\sin^3\theta\partial_{x'x'}j_{y'}-3\sin^2\theta\cos\theta\partial_{x'y'}j_{y'}, \\ \partial_{xx} j_y = -3\cos\theta\sin^2\theta\partial_{x'y'}j_{x'}+\sin^3\theta\partial_{y'y'}j_{x'} \\ \qquad +\cos^3\theta\partial_{x'x'}j_{y'}-3\cos^2\theta\sin\theta\partial_{x'y'}j_{y'}, \\ \partial_{xy} j_y = -\sin\theta(\sin^2\theta-2\cos^2\theta)\partial_{x'y'}j_{x'} - \cos\theta\sin^2\theta\partial_{y'y'}j_{x'} \\ \qquad +\cos^2\theta\sin\theta\partial_{x'x'}j_{y'}+\cos\theta(\cos^2\theta-2\sin^2\theta)\partial_{x'y'}j_{y'}. \end{cases} \tag{A.3}$$

A.2 Cylindrical coordinate system

For the sake of completeness, this section summarizes the mathematical apparatus underpinning the mapping between *Cartesian to cylindrical* systems $(y,z)\mapsto(r,\theta)$, and vice-versa $(r,\theta)\mapsto(y,z)$, given by:

$$\begin{cases} y = r\cos\theta, \\ z = r\sin\theta, \end{cases} \qquad \begin{cases} r = \sqrt{y^2+z^2}, \\ \theta = \arctan(z/y). \end{cases} \tag{A.4}$$

Considering the mapping $(y,z)\mapsto(r,\theta)$, the relations between first- and second-order momentum derivatives are expressed as follows:

$$\begin{cases} \partial_y j_x = \cos\theta\partial_r j_x - \frac{1}{r}\sin\theta\partial_\theta j_x, \\ \partial_z j_x = \sin\theta\partial_r j_x + \frac{1}{r}\cos\theta\partial_\theta j_x, \end{cases} \tag{A.5a}$$

$$\begin{cases} \partial_{xx} j_x = \cos^2\theta\partial_{rr}j_x+\frac{1}{r}\sin^2\theta\partial_r j_x-\frac{1}{r}\sin2\theta\partial_{r\theta}j_x+\frac{1}{r^2}\sin2\theta\partial_\theta j_x+\frac{1}{r^2}\sin^2\theta\partial_{\theta\theta}j_x, \\ \partial_{yy} j_x = \sin^2\theta\partial_{rr}j_x+\frac{1}{r}\cos^2\theta\partial_r j_x+\frac{1}{r}\sin2\theta\partial_{r\theta}j_x-\frac{1}{r^2}\sin2\theta\partial_\theta j_x+\frac{1}{r^2}\cos^2\theta\partial_{\theta\theta}j_x, \\ \partial_{yz} j_x = \frac{1}{2}\sin2\theta\partial_{rr}j_x-\frac{1}{2r}\sin2\theta\partial_r j_x+\frac{1}{r}\cos2\theta\partial_{r\theta}j_x-\frac{1}{r^2}\cos2\theta\partial_\theta j_x-\frac{1}{2r^2}\sin2\theta\partial_{\theta\theta}j_x. \end{cases} \tag{A.5b}$$

Conversely, the mapping between *cylindrical to Cartesian* systems $(r,\theta)\mapsto(y,z)$ reads as follows:

$$\begin{cases}\partial_r j_x=\cos\theta\partial_y j_x+\sin\theta\partial_z j_x,\\ \partial_{rr} j_x=-\frac{1}{r^2}\partial_{\theta\theta} j_x-\frac{1}{r}\partial_r j_x+\left(\partial_{yy} j_x+\partial_{zz} j_x\right)\\ \qquad=\cos^2\theta\partial_{yy} j_x+\sin^2\theta\partial_{zz} j_x+\sin2\theta\partial_{yz} j_x,\\ \partial_\theta j_x=-r\sin\theta\partial_y j_x+r\cos\theta\partial_z j_x,\\ \partial_{\theta\theta} j_x=-r\partial_r j_x+r^2\left(\sin^2\theta\partial_{yy} j_x+\cos^2\theta\partial_{zz} j_x-\sin2\theta\partial_{yz} j_x\right),\\ \partial_{r\theta} j_x=\frac{1}{r}\partial_\theta j_x+r\left(\frac{1}{2}\sin2\theta\left(-\partial_{yy} j_x+\partial_{zz} j_x\right)+\cos2\theta\partial_{yz} j_x\right).\end{cases}\tag{A.6}$$

B Derivation of Eq. (6.2b)

The derivation of Eq. (6.2b) proceeds along the following steps. We start by expanding Eq. (3.3b), taking into account that we are dealing with a 2D planar channel geometry; the result reads:

$$\hat{n}_q^-=-t_q c_{qx}\left(3c_{qy}^2-1\right)\partial_y\left(\nu\partial_y j_x\right)=-t_q c_{qx}\left(3c_{qy}^2-1\right)\left[\partial_y\nu\partial_y j_x+\nu\partial_{yy} j_x\right].\tag{B.1}$$

Next, we need to assess the term $\partial_y\nu$. For that, we use Eq. (4.2) as rheological model, which produces the following result:

$$\begin{aligned}\partial_y\nu=&\partial_y\left(\nu_\infty+a\left|\partial_y j_x\right|^{n-1}\right)\\ =&a(n-1)\left(\partial_y j_x\right)\left|\partial_y j_x\right|^{n-3}\partial_{yy} j_x\\ =&(\nu-\nu_\infty)(n-1)\frac{1}{\partial_y j_x}\partial_{yy} j_x.\end{aligned}\tag{B.2}$$

Finally, we introduce Eq. (B.2) into Eq. (B.1), which leads to Eq. (6.2b).

C Derivation of Eq. (6.11b)

The derivation of Eq. (6.11b) proceeds along the following steps. We start by expanding Eq. (3.3b), restricted to a 2D domain; the result reads:

$$\begin{aligned}\hat{n}_q^-=&-t_q c_{qx}\left(3c_{qy}^2-1\right)\left[\partial_x\left(\nu\partial_y j_y\right)+\partial_y\left(\nu\partial_x j_y+\nu\partial_y j_x\right)\right]\\ &-t_q c_{qy}\left(3c_{qx}^2-1\right)\left[\partial_y\left(\nu\partial_x j_x\right)+\partial_x\left(\nu\partial_x j_y+\nu\partial_y j_x\right)\right].\end{aligned}\tag{C.1}$$

Like in Eq. (B.1), the spatial derivatives in Eq. (C.1) are expanded as follows:

$$\begin{aligned}\hat{n}_q^-=&-t_q c_{qx}\left(3c_{qy}^2-1\right)\left[\partial_x\nu\partial_y j_y+\partial_y\nu\left(\partial_x j_y+\nu\partial_y j_x\right)+\nu\left(\partial_{yy} j_x+2\partial_{xy} j_y\right)\right]\\ &-t_q c_{qy}\left(3c_{qx}^2-1\right)\left[\partial_y\nu\partial_x j_x+\partial_x\nu\left(\partial_x j_y+\nu\partial_y j_x\right)+\nu\left(\partial_{xx} j_y+2\partial_{xy} j_x\right)\right].\end{aligned}\tag{C.2}$$

To proceed forward it is useful to introduce the mapping between fixed and rotated Cartesian systems $(x,y)\mapsto(x',y')$, which is detailed in Appendix A.1. Then, we take into consideration that (x',y') locally aligns with the wall tangential and normal directions, respectively, as sketched in Fig. 2. Developing Eq. (C.2) on this (x',y') coordinate system and recognizing that we are dealing with a 2D channel geometry, we can assume the flow streamwise invariance, which translates to $\partial_{x'}=0$ (note that a similar condition was invoked in Appendix B). Operating this set of changes into Eq. (C.2) we obtain:

$$\begin{aligned}\hat{n}_q^- =&-t_q\left[\left(3c_{qy}^2-1\right)c_{qx}\cos\theta\left(\cos^2\theta-2\sin^2\theta\right)\right.\\&\left.+\left(3c_{qx}^2-1\right)c_{qy}\sin\theta\left(\sin^2\theta-2\cos^2\theta\right)\right]\left[\partial_{y'}\nu\partial_{y'}j_{x'}+\nu\partial_{y'y'}j_{x'}\right].\end{aligned}\tag{C.3}$$

Following Appendix B, we can map Eq. (B.2) onto the (x',y') frame, which leads to $\partial_{y'}\nu\partial_{y'}j_{x'}=(\nu-\nu_\infty)(n-1)\partial_{y'y'}j_{x'}$. This result is finally substituted into Eq. (C.3). In the end, Eq. (C.3) boils down to Eq. (6.11b).

D Derivation of Eq. (6.15b)

The derivation of Eq. (6.2b) proceeds along the following steps. We start by expanding Eq. (6.15b), taking into account that we are dealing with a 3D circular tube geometry; the result reads:

$$\begin{aligned}\hat{n}_q^- =&-t_q c_{qx}\left[\left(3c_{qy}^2-1\right)\partial_y\left(\nu\partial_y j_x\right)+\left(3c_{qz}^2-1\right)\partial_z\left(\nu\partial_z j_x\right)\right]\\=&-t_q c_{qx}\left[\left(3c_{qy}^2-1\right)\left(\partial_y\nu\partial_y j_x+\nu\partial_{yy}j_x\right)+\left(3c_{qz}^2-1\right)\left(\partial_z\nu\partial_z j_x+\nu\partial_{zz}j_x\right)\right]\\=&-t_q c_{qx}\left[\left(3c_{qy}^2-1\right)\left(\left[\cos^2\theta\partial_r\nu+\nu\frac{1}{r}\sin^2\theta\right]\partial_r j_x+\nu\cos^2\theta\partial_{rr}j_x\right)\right.\\&\left.+\left(3c_{qz}^2-1\right)\left(\left[\sin^2\theta\partial_r\nu+\nu\frac{1}{r}\cos^2\theta\right]\partial_r j_x+\nu\sin^2\theta\partial_{rr}j_x\right)\right].\end{aligned}\tag{D.1}$$

The last equality is obtained based on the following identities: $\partial_y j_x=\cos\theta\partial_r j_x$, $\partial_z j_x=\sin\theta\partial_r j_x$, $\partial_{yy}j_x=\cos^2\theta\partial_{rr}j_x+\frac{1}{r}\sin^2\theta\partial_r j_x$, and $\partial_{zz}j_x=\sin^2\theta\partial_{rr}j_x+\frac{1}{r}\cos^2\theta\partial_r j_x$, with $\partial_\theta j_x=0$ implied based on circumferential invariance; recall the general relationships in Appendix A.

Next, we assess the term $\partial_r\nu$. Similarly to Eq. (B.2), the $\partial_r\nu$ term can be expressed as follows:

$$\begin{aligned}\partial_r\nu=&\partial_r\left(\nu_\infty+a\left|\partial_r j_x\right|^{n-1}\right)\\=&a(n-1)\left(\partial_r j_x\right)\left|\partial_r j_x\right|^{n-3}\partial_{rr}j_x\\=&(\nu-\nu_\infty)(n-1)\frac{1}{\partial_r j_x}\partial_{rr}j_x.\end{aligned}\tag{D.2}$$

Then, we introduce Eq. (D.2) into Eq. (D.1), which leads to:

$$\begin{aligned}\hat{n}_q^- = -t_q c_{qx}\Bigg[&\left(3c_{qy}^2-1\right)\Bigg(\left[(n-1)(\nu-\nu_\infty)+\nu\right]\left(\cos^2\theta\,\partial_{rr}j_x+\frac{1}{r}\sin^2\theta\,\partial_r j_x\right)\\&-(n-1)(\nu-\nu_\infty)\frac{1}{r}\sin^2\theta\,\partial_r j_x\Bigg)\\&+\left(3c_{qz}^2-1\right)\Bigg(\left[(n-1)(\nu-\nu_\infty)+\nu\right]\left(\sin^2\theta\,\partial_{rr}j_x+\frac{1}{r}\cos^2\theta\,\partial_r j_x\right)\\&-(n-1)(\nu-\nu_\infty)\frac{1}{r}\cos^2\theta\,\partial_r j_x\Bigg)\Bigg].\end{aligned} \tag{D.3}$$

Finally, we re-express the momentum derivatives in Eq. (D.3) in cartesian coordinates, using the relations $\partial_r j_x = \cos\theta\,\partial_y j_x + \sin\theta\,\partial_z j_x$ and $\partial_{rr} j_x = -\frac{1}{r}\partial_r j_x + \left(\partial_{yy} j_x + \partial_{zz} j_x\right)$, subject to the assumption of circumferential invariance; recall the general relationships in Appendix A. The end result produces Eq. (6.15b).

E Derivation of $\partial_\theta j_{\rm ws}$ and $\partial_{\theta\theta} j_{\rm ws}$ in Eq. (6.17)

This section presents the explicit content of $\partial_\theta j_{\rm ws}$ and $\partial_{\theta\theta} j_{\rm ws}$, which can be found in the kinematic constraint conditions of the slip velocity boundary schemes presented in Eq. (6.17) of Section 5. From the computational implementation standpoint, all variables shown here are obtainable by the previous time step solution. Numerically, it was confirmed that stable and unique steady-state solutions can be obtained through this procedure.

Navier non-linear (NNL) slip velocity model:

$$\partial_\theta j_{\rm ws} = k_{nl}\left|\nu\,\partial_r j_x\right|^{m-2}\left[\left|\nu\,\partial_r j_x\right|+(m-1)\,\nu\,\mathrm{sgn}\left(\nu\,\partial_r j_x\right)\partial_r j_x\right]\left(\partial_\theta\nu\,\partial_r j_x+\nu\,\partial_{r\theta} j_x\right)\Big|_{\boldsymbol{x}_w}. \tag{E.1}$$

Asymptotic (ASP) slip velocity model:

$$\partial_\theta j_{\rm ws} = \frac{k_{a1}k_{a2}}{1+k_{a2}\nu\,\partial_r j_x}\left(\partial_\theta\nu\,\partial_r j_x+\nu\,\partial_{r\theta} j_x\right)\Big|_{\boldsymbol{x}_w}. \tag{E.2}$$

Hatzikiriakos (HZK) slip velocity model:

$$\partial_\theta j_{\rm ws} = k_{h1}k_{h2}\cosh\left(k_{h2}\nu\,\partial_r j_x\right)\left(\partial_\theta\nu\,\partial_r j_x+\nu\,\partial_{r\theta} j_x\right)\Big|_{\boldsymbol{x}_w}. \tag{E.3}$$

In the above equations, the term $\partial_\theta\nu$ at $\boldsymbol{x}_w$, when viscosity ν obeys the Sisko model, Eq. (4.3), is given by:

$$\partial_\theta\nu(\boldsymbol{x}_w) = a(n-1)\left|\partial_r j_x\right|^{n-2}\mathrm{sgn}\left(\partial_r j_x\right)\partial_{r\theta} j_x\Big|_{\boldsymbol{x}_w}. \tag{E.4}$$

The derivation procedure finishes with the replacement of the momentum derivatives from cylindrical to cartesian coordinate systems. To this end, we employ the relationships shown in Appendix A, namely: $\partial_r j_x = \cos\theta\partial_y j_x + \sin\theta\partial_z j_x$ and $\partial_{r\theta} j_x = \frac{1}{r}\partial_\theta j_x + r\left(\frac{1}{2}\sin 2\theta\left(-\partial_{yy} j_x + \partial_{zz} j_x\right) + \cos 2\theta\partial_{yz} j_x\right)$. These momentum derivatives are readily available from the previous time step solution(s).

As for the term $\partial_{\theta\theta} j_{\text{ws}}$, this term may be neglected, regardless the slip velocity boundary model, as it features higher-order derivatives or products of higher-order derivative terms. Hence, in general, we may consider $\partial_{\theta\theta} j_{\text{ws}} = 0$.

References

[1] Sharipov, F., Seleznev, V. Data on Internal Rarefied Gas Flows. J. Phys. Chem. Ref. Data 27, 657–706, 1998. (doi: 10.1063/1.556019)

[2] Lockerby, D.A., Reese, J.M., Emerson, D.R., and Barber, R.W. Velocity boundary condition at solid walls in rarefied gas calculations. Phys. Rev. E, 70, 017303, 2004. (doi: 10.1103/PhysRevE.70.017303)

[3] Zhang, W.-M., Meng, G., Wei, X. A review on slip models for gas microflows. Microfluid Nanofluid 13, 845–882, 2012. (doi: 10.1007/s10404-012-1012-9)

[4] Ya Malkin, A., Patlazhan, S. A. Wall slip for complex liquids – Phenomenon and its causes. Adv. Colloid Interface Sci. 257, 42–57, 2018. (doi: 10.1016/j.cis.2018.05.008)

[5] Rothstein, J. P. Slip on Superhydrophobic Surfaces. Ann. Rev. Fluid Mech. 42, 89, 2010. (doi: 10.1146/annurev-fluid-121108-145558)

[6] Wang, G. J., Hadjiconstantinou, N. G. Universal molecular-kinetic scaling relation for slip of a simple fluid at a solid boundary. Phys. Rev. Fluids 4, 064201, 2019. (doi: 10.1103/PhysRevFluids.4.064201)

[7] Hadjiconstantinou N. G., Molecular Mechanics of Liquid and Gas Slip Flow. Ann. Rev. Fluid Mech. 56, 435, 2024. (doi: 10.1146/annurev-fluid-121021- 014808)

[8] Karniadakis, G., Beskok, A., Aluru, N. Microflows and Nanoflows: Fundamentals and Simulation, Springer-Verlag New York, 2005. (doi: 10.1007/0-387-28676-4)

[9] Lauga E., Brenner M., Stone, H. Microfluidics: The No-Slip Boundary Condition. Springer Handbooks. Eds C. Tropea, A.L. Yarin and J.F. Foss, Springer, 2007. (doi: 10.1007/978-3-540-30299-5_19)

[10] Sone, Y. Kinetic Theory and Fluid Dynamics. Birkhäuser, Boston, 2002. (doi: 10.1007/978-1-4612-0061-1)

[11] Maxwell, J. C. On stresses in rarified gases arising from inequalities of temperature. Philos. Trans. R. Soc. London 170, 231-256, 1879. (doi: 10.1098/rstl.1879.0067)

[12] Guo, Z., Qin, J, Chuguang, C. Generalized second-order slip boundary condition for nonequilibrium gas flows. Phys. Rev. E 89, 013021, 2014. (doi: 10.1103/PhysRevE.89.013021)

[13] Gad-el-Hak M. The fluid mechanics of microdevices — the Freeman Scholar lecture. J. Fluids Eng. 121, 5–33, 1999. (doi: 10.1115/1.2822013)

[14] Li, Z., Li, J., Yan, G., Galindo-Torres, S., Scheuermann, A., Li, L. Mesoscopic model framework for liquid slip in a confined parallel-plate flow channel. Phys. Rev. Fluids 6, 034203, 2021. (doi: 10.1146/annurev-fluid-121108-145558)

[15] Tretheway, D. C., Meinhart, C. D. Apparent fluid slip at hydrophobic microchannel walls, Phys. Fluids 14, L9, 2002. (doi: 10.1063/1.1432696)

[16] Ferrás, L. L., Nóbrega, J. M., Pinho, F. T. Analytical solutions for Newtonian and inelastic Non-newtonian flows with wall slip. J. Non-Newtonian Fluid Mech. 175-176, 76–88, 2012. (doi: 10.1016/j.jnnfm.2012.03.004)
[17] Panaseti, P., Georgiou, G. C. Viscoplastic flow development in a channel with slip along one wall. J. Non-Newtonian Fluid Mech. 248, 8-22, 2017. (doi: 10.1016/j.jnnfm.2017.08.008)
[18] Liakos, A. Discretization of the Navier-Stokes equations with slip boundary condition. Numerical Methods for Partial Differential Equations 17, 26–42, 2001. (doi: 10.1002/1098-2426(200101)17:1<26::AID-NUM2>3.0.CO;2-D)
[19] Araya, R., Caiazzo, A., Chouly, F. Stokes problem with slip boundary conditions using stabilized finite elements combined with Nitsche. Comput. Methods Appl. Math. 427, 117037, 2024. (doi: 10.1016/j.cma.2024.117037)
[20] Ferrás, L. L., Nóbrega, J. M., Pinho, F. T. Implementation of slip boundary conditions in the finite volume method: new techniques. Int. J. Numer. Meth. Fluids. 72, 724, 2013. (doi: 10.1002/fld.3765).
[21] ANSYS Polyflow manual (implementation of boundary conditions), ANSYS, 2011.
[22] Aidun, C. K., Clausen, J.R. Lattice-Boltzmann method for complex flows. Annu. Rev. Fluid Mech. 42, 439, 2010. (doi: 10.1146/annurev-fluid-121108-145519)
[23] Succi, S. The Lattice Boltzmann Equation: For Complex States of Flowing Matter. Oxford University Press, 2018. (doi: 10.1093/oso/9780199592357.001.0001)
[24] Krüger, T., Kusumaatmaja, H., Kuzmin, A., Shardt, O., Silva, G., Viggen, E. M. The Lattice Boltzmann Method – Principles and Practice. 1st ed., Springer, 2016. (doi: 10.1007/978-3-319-44649-3)
[25] Ansumali, S., Karlin, I. V. Kinetic boundary conditions in the lattice Boltzmann method. Phys. Rev. E 66, 026311, 2002. (doi: 10.1103/PhysRevE.66.026311)
[26] Guo, Z., Shi, B., Zhao, T. S., Zheng, C. Discrete effects on boundary conditions for the lattice Boltzmann equation in simulating microscale gas flows. Phys. Rev. E 76, 056704, 2007. (doi: 10.1103/PhysRevE.76.056704)
[27] Guo, Z., Zheng, C. Analysis of lattice Boltzmann equation for microscale gas flows: Relaxation time, Boundary condition, and Knudsen layer. Int. J. Comput. Fluid Dyn. 22, 465, 2008. (doi: 10.1080/10618560802253100)
[28] Verhaeghe, F., Luo, L.-S., Blanpain, B. Lattice Boltzmann modeling of microchannel flow in slip flow regime. J. Comput. Phys. 228, 147, 2009. (doi: 10.1016/j.jcp.2008.09.004)
[29] Prasianakis, N., Ansumali, S. Microflow Simulations via the Lattice Boltzmann Method. Commun. Comput. Phys. 9, 1128-1136, 2011. (doi: 10.4208/cicp.301009.271010s)
[30] Reis, T., Dellar, P. J. Lattice Boltzmann simulations of pressure-driven flows in microchannels using Navier–Maxwell slip boundary conditions. Phys. Fluids 24, 112001, 2012. (doi: 10.1063/1.4764514)
[31] Tao, S., Guo, Z. Boundary condition for lattice Boltzmann modeling of microscale gas flows with curved walls in the slip regime. Phys. Rev. E 91, 043305, 2015. (doi: 10.1103/PhysRevE.91.043305)
[32] Wang, L., Yin, X. Apparent permeability of flow through periodic arrays of sphereswith first-order slip. Powder Technol. 311, 313, 2017. (doi: 10.1016/j.powtec.2017.01.072)
[33] Silva, G., Semiao, V. Consistent lattice Boltzmann modeling of low-speed isothermal flows at finite Knudsen numbers in slip-flow regime: Application to plane boundaries. Phys. Rev. E 96, 013311, 2017. (doi: 10.1103/PhysRevE.96.013311)
[34] Silva, G. Consistent lattice Boltzmann modeling of low-speed isothermal flows at finite Knudsen numbers in slip-flow regime. II. Application to curved boundaries. Phys. Rev. E

98, 023302, 2018. (doi: 10.1103/PhysRevE.98.023302)
[35] Wang, L., Tao, S., Hu, J., Zhang, K., Lu, G. Curved boundary conditions of the lattice Boltzmann method for simulating microgaseous flows in the slip flow regime. Comput. Fluids 230, 105117, 2021. (doi: 10.1016/j.compfluid.2021.105117)
[36] Mohammed, S., Reis, T. Lattice Boltzmann method with moment-based boundary conditions for rarefied flow in the slip regime. Phys. Rev. E 104, 045309, 2021. (doi: 10.1103/PhysRevE.104.045309)
[37] Silva, G., Ginzburg, I. Slip Velocity Boundary Conditions for the Lattice Boltzmann Modeling of Microchannel Flows. Int. J. Numer. Methods Fluids 94, 2104, 2022. (doi: 10.1002/fld.5138)
[38] Pereira G. G., Kuang S., Chai Z., Shi B. A Pseudopotential Lattice Boltzmann Analysis for Multicomponent Flow Yong Zhao. Commun. Comput. Phys. 32, 1156, 2022. (doi:10.4208/cicp.OA-2022-0209)
[39] Datadien K, P. N., Di Staso G., Diddens C., Wijshoff H. M. A., Toschi F. Comparison of Lattice Boltzmann, Finite Element and Volume of Fluid Multicomponent Methods for Microfluidic Flow Problems and the Jetting of Microdroplets. Commun. Comput. Phys. 33, 912-936, 2023. (doi: 10.4208/cicp.OA-2022-0181)
[40] Guo Z., Asinari P., Zheng C. Lattice Boltzmann equation for microscale gas flows of binary mixtures. Phys. Rev. E 79, 026702, 2009. (doi: 10.1103/PhysRevE.79.026702)
[41] Yang, L., Yu, Y., Hou, G., Wang, K., Xiong, Y. Boundary conditions with adjustable slip length for the lattice Boltzmann simulation of liquid flow. Comput. Fluids 174, 200–212, 2018. (doi: 10.1016/j.compfluid.2018.08.002)
[42] Aminpour, M., Galindo-Torres, S. A., Scheuermann, A., Li, L. Slip-flow lattice-Boltzmann simulations in ducts and porous media: A full rehabilitation of spurious velocities. Phys. Rev. E 98, 043110, 2018. (doi: 10.1103/PhysRevE.98.043110)
[43] Navier, C. L. M. Sur les lois du Mouvement des Fluides. Mem. Acad. Roy. Sci. Inst. Fr. 6, 389–440, 1827. (doi: 10.1063/1.556019)
[44] Bird, R. B. Useful non-Newtonian models. Annual Review of Fluid Mechanics 8, 13-34, 1976. (doi: 10.1146/annurev.fl.08.010176.000305)
[45] Chhabra, R. P., Richardson, J.F. Non-Newtonian Flow and Applied Rheology. 2nd ed., Butterworth-Heinemann, 2008. (doi: 10.1016/B978-0-7506-8532-0.X0001-7)
[46] Sisko, A. W. Flow of lubricating greases. Ind. Eng. Chem. 50, 12, 1789–1792, 1958. (doi: 10.1021/ie50588a042)
[47] de Waele, A. Viscometry and plastometry. J. Oil. Color Chem. Assoc. J. 6, 33–88, 1923.
[48] Gabbanelli, S., Drazer, G., Koplik, J. Lattice Boltzmann method for non-Newtonian (power-law) fluids. Phys. Rev. E 72, 046312, 2005. (doi: 10.1103/PhysRevE.72.046312)
[49] Boyd, J., Buick, J., Green, S. A second-order accurate lattice Boltzmann non-Newtonian flow model. Journal of Physics A 39, 14241–14247, 2006. (doi: 10.1088/0305-4470/39/46/001)
[50] Malaspinas, O., Courbebaisse, G., Deville, M.O. Simulation of generalized Newtonian fluids with the lattice Boltzmann method. Int. J. of Mod. Phys. C 18, 1939–1949, 2007. (doi: 10.1142/S0129183107011832)
[51] Malaspinas, O., Fiétier, N., Deville, M. Lattice Boltzmann method for the simulation of viscoelastic fluid flows. J. Non-Newtonian Fluid Mech. 165, 1637–1653, 2010. (doi: 10.1016/j.jnnfm.2010.09.0012)
[52] Lugarini, A., Admilson, T. F., Philippi, P. C. Lattice Boltzmann method for viscoplastic fluid flow based on regularization of ghost moments. J. Non-Newtonian Fluid Mech. 282, 104413, 2020. (doi: 10.1016/j.jnnfm.2020.104413)

[53] Gsell, S., D'Ortona, U., Favier, J. Lattice-Boltzmann simulation of creeping generalized Newtonian flows: Theory and guidelines. J. Comput. Phys. 429, 109943, 2021. (doi: 10.1016/10.1016/j.jcp.2020.109943)
[54] Vikhansky, A. Lattice-Boltzmann method for yield-stress liquids. J. Non-Newtonian Fluid Mech. 155 (3), 95–100, 2008. (doi: 10.1016/j.jnnfm.2007.09.001)
[55] Chai, Z., Shi, B., Guo, Z., Rong, F. Multiple-relaxation-time lattice Boltzmann model for generalized Newtonian fluid flows. J. Non-Newtonian Fluid Mech. 166, 332-342, 2011. (doi: 10.1016/j.jnnfm.2011.01.002)
[56] Li, Q., Hong, N., Shi, B., Chai, Z. Simulation of power-law fluid flows in two-dimensional square cavity using multi-relaxation-time lattice Boltzmann method. Commun Comput Phys 15, 265-284, 2014. (doi: 10.4208/cicp.160212.210513a)
[57] Grasinger, M., Overacker, S., Brigham, J. Numerical investigation of the accuracy, stability, and efficiency of lattice Boltzmann methods in simulating non-Newtonian flow. Comput Fluids 166, 253–274, 2018. (doi: 10.1016/j.compfluid.2018.02.008)
[58] Adam, S., Premnath, K. N. Numerical investigation of the cascaded central moment lattice Boltzmann method for non-Newtonian fluid flows. J. Non-Newtonian Fluid Mech. 274, 104188, 2019. (doi: 10.1016/j.jnnfm.2019.104188)
[59] Adam, S., Hajabdollahi, F., Premnath, K. N. Cascaded lattice Boltzmann modeling and simulations of three-dimensional non-Newtonian fluid flows. Comput. Phys. Commun. 262, 107858, 2021. (doi: 10.1016/j.cpc.2021.107858)
[60] Yoshino, M., Hotta, Y.-h., Hirozane, T., Endo, M. A numerical method for incompressible non-Newtonian fluid flows based on the lattice Boltzmann method. J. Non-Newtonian Fluid Mech. 147: 69-78, 2007. (doi: 10.1016/j.jnnfm.2007.07.007)
[61] Ginzbourg I., Adler P. M. Boundary flow condition analysis for the three-dimensional lattice Boltzmann model. J. Phys. II Fr. 4, 191–214, 1994. (doi: 10.1051/jp2:1994123)
[62] Ginzburg, I., d'Humières, D. Multi-reflection boundary conditions for lattice Botlzmann models. Phys. Rev. E 68, 066614, 2003. (doi: 10.1103/PhysRevE.68.066614)
[63] d'Humières, D., Ginzburg, I. Viscosity independent numerical errors for Lattice Boltzmann models: From recurrence equations to "magic" collision numbers. Comput. Math. Appl. 58, 823, 2009. (doi: 10.1016/j.camwa.2009.02.008)
[64] Ginzburg, I., Verhaeghe, F., d'Humières, D. Two-relaxation-time lattice Boltzmann scheme: about parametrization, velocity, pressure and mixed conditions. Commun. Comp. Phys.3, 427, 2008.
[65] Ginzburg, I. Consistent lattice Boltzmann schemes for the Brinkman model of porous flow and infinite Chapman-Enskog expansion. Phys. Rev. E 77, 066704, 2008. (doi: 10.1103/PhysRevE.77.066704)
[66] Khirevich, S., Ginzburg, I., Tallareka, U. Coarse-and fine-grid numerical behavior of MRT/TRT lattice-Boltzmann schemes in regular and random sphere packings. J. Comput. Phys. 281, 708–742, 2015. (doi: 10.1016/j.jcp.2014.10.038)
[67] Ginzburg, I., d'Humières, D. Local second-order boundary method for lattice Botlzmann models. J. Stat. Phys. 64, 927–971, 1996. (doi: 10.1007/BF02174124)
[68] Ginzburg, I., d'Humières, D. Local second-order boundary method for lattice Botlzmann models. Part II. Application to Poisson equation in complicated geometries. Unpublished, 1995.
[69] Silva, G., Ginzburg, I. Reviving the local second-order boundary approach within the two-relaxation-time lattice Boltzmann modelling. Phil. Trans. R. Soc. A 378, 20190404, 2020. (doi: 10.1098/rsta.2019.0404)

[70] Schowalter, W. R. The behavior of complex fluids at solid boundaries. J. Non-Newtonian Fluid Mech. 29, 25–36, 1988. (doi: 10.1016/0377-0257(88)85048-1)
[71] Hatzikiriakos, S. G. A slip model for linear polymers based on adhesive failure. Intern. Polym. Process. 8, 135–142, 1993. (doi: 10.3139/217.930135)
[72] Happel J., Brenner H. Low Reynolds number hydrodynamics with applications to particulate media. Prentice-Hall, Englewood Cliffs, NJ, 1965.
[73] Ginzburg, I. Truncation errors, exact and heuristic stability analysis of two-relaxation-times lattice Boltzmann schemes for anisotropic advection–diffusion equation. Commun. Comput. Phys. 11(5), 1439–1502, 2012. (doi: 10.4208/cicp.211210.280611a)
[74] Chapman, S., Cowling, T. The Mathematical Theory of Non-Uniform Gases. 3rd. ed., Cambridge Univ. Press, 1970.
[75] Silva G. Discrete effects on the forcing term for the lattice Boltzmann modeling of steady hydrodynamics. Comput. Fluids 203, 104537, 2020. (doi: 10.1016/j.compfluid.2020.104537)
[76] Postma B., Silva G. Force methods for the two-relaxation-times lattice Boltzmann. Phys. Rev. E 102, 063307, 2021. (doi: 10.1103/PhysRevE.102.063307)
[77] Silva G. Discrete effects on the source term for the lattice Boltzmann modeling of one-dimensional reaction–diffusion equations. Comput. Fluids 251, 105735, 2023. (doi: 10.1016/j.compfluid.2022.105735)
[78] Talon, L., Bauer, D., Gland, N., Youssef, S., Auradou, H., Ginzburg, I. Assessment of the two relaxation time Lattice-Boltzmann scheme to simulate Stokes flow in porous media. Water Resour. Res. 48, W04526, 2012. (doi: 10.1029/2011WR011385)
[79] Ginzburg, I. Steady-state two-relaxation-time lattice Boltzmann formulation for transport and flow, closed with the compact multi-reflection boundary and interface-conjugate schemes. J. Comput. Sci. 54, 101215, 2021. (doi: 10.1016/j.jocs.2020.101215)
[80] Krüger, T., Varnik, F., Raabe, D. Shear stress in lattice Boltzmann simulations. Phys. Rev. E 79, 046704, 2009.
[81] Qian, Y. H., d'Humières, D., Lallemand, P. Lattice BGK models for Navier–Stokes equation, Europhys. Lett. 17(6), 479, 1992. (doi: 10.1209/0295-5075/17/6/001)
[82] Zou, Q., He, X. On pressure and velocity boundary conditions for the lattice Boltzmann BGK model. Phys. Fluids. 9, 1592–1598, 1997. (doi: 10.1063/1.869307)
[83] Silva, G., Leal, N., Semiao, V. Determination of microchannels geometric parameters using micro-PIV. Chemical Engineering Research and Design 87, 298–306, 2009. (doi: j.cherd.2008.08.009)
[84] Ternik, P. Planar sudden symmetric expansion flows and bifurcation phenomena of purely viscous shear-thinning fluids. Journal of Non- Newtonian Fluid Mechanics 157, 15-25, 2009. (doi: 10.1016/j.jnnfm.2008.09.002)
[85] Manica, R., Bortoli, A. Simulation of sudden expansion flows for power-law fluids, Journal of Non-Newtonian Fluid Mechanics 121, 35-40, 2004. (doi: 10.1016/j.jnnfm.2004.03.009)
[86] Ginzburg, I., Steiner, C. Lattice Boltzmann model for free-surface flow and its applicationto filling process in casting. J. Comput. Phys. 185, 61–99, 2003. (doi:10.1016/S0021-9991(02)00048-7)
[87] Malaspinas, O., Chopard, B., Latt, J. General regularized boundary condition for multi-speed lattice Boltzmann models. Comput. Fluids 49, 29-35, 2011. (doi:10.1016/j.compfluid.2011.04.010)
[88] Zhang, L., Zeng, Z., Xie, H., Tau, X., Zhang, Y., Lu, Y., Yoshikawa, A., Kawazoe, Y. An alternative second order scheme for curved boundary condition in lattice Boltzmann method. Comput. Fluids. 144, 193-202, 2015. (doi:10.1016/j.compfluid.2015.03.006)

[89] Ginzburg, I, Silva, G., Marson, F., Chopard, B., Latt, J. Unified directional parabolic-accurate lattice Boltzmann boundary schemes for grid-rotated narrow gaps and curved walls in creeping and inertial fluid flows. Phys. Rev. E 107, 025303, 2023. (doi: 10.1103/PhysRevE.107.025303)

[90] Ginzburg, I, Silva G. Mass-balance and locality versus accuracy with the new boundary and interface- conjugate approaches in advection-diffusion lattice Boltzmann method. Phys Fluids 33(5):57104, 2021. (doi: 10.1063/5.0047210)